LA-UR-23-34026

Approved for public release; distribution is unlimited.

Title:	RANS Simulation of Variable Density Turbulent Round Jets with Coflow using xRAGE Hydrodynamic Code and BHR Turbulence Models
Author(s):	Ji, Minsuk
Intended for:	Report
Issued:	2023-12-15

RANS Simulation of Variable Density Turbulent Round Jets with Coflow using xRAGE Hydrodynamic Code and BHR Turbulence Models

Minsuk Ji

November 6, 2023

1 Background

This work for the fiscal year 2023 (FY23) is a continuation of previous efforts to evaluate the BHR turbulence models [1, 2, 3, 4] for their ability to accurately simulate variable density turbulent round jets with coflow [5]. As before, RANS simulations are carried out using the xRAGE hydrodynamic code. The following are some of the previous findings. Israel [6] showed that i) the symmetry boundary conditions for the BHR models in axisymmetric simulations were in error, ii) three grids of different resolutions did not lead to converging solutions, and iii) BHR 3.1 simulation exhibited instabilities and did not reach a steady state. Saenz and Rauenzahn [7] derived and implemented into xRAGE the correct BHR boundary conditions at the symmetry axis. Cline [8] conducted sensitivity studies with various parameters including the BHR models (versions 2, 3.1 and 4), gravity, material pressure, specific heat, initial turbulent kinetic energy and initial turbulent length scale, and found that the largest factor impacting on simulation results was the BHR model version, followed by the initial turbulent length scale. In addition, freeze boundary conditions at the exit and the side wall of the computational domain were used to remove anomalous flow behavior. Cline [9] adjusted the inlet jet velocity, initial turbulent kinetic energy and initial turbulent length scale to obtain the best reasonable match with the experimental data of Charonko and Prestridge [5]. It was found that the BHR 2 and 3.1 models performed in a similar manner, but the BHR 2 model produced much lower levels of density-specific-volume covariance and turbulent kinetic energy.

The main focus for the FY23 is to study the effects of computational parameters related to the boundary conditions, mesh, domain size and timestep size. The reasoning behind this is that, unless simulation results can be shown to be reasonably independent from the aforementioned computational parameters, it would be difficult to attribute any discrepancies between simulation and experimental results to turbulence models. This important aspect has largely been overlooked in the previous years, and therefore will be studied comprehensively here. Additionally, effects of varying the initial turbulent length scale will be examined because it was previously [8] identified as a major factor affecting the flow fields.

2 Computational Setup

2.1 Flow Domain

Figure 1 shows the experimental setup of Charonko and Prestridge [5] on the left, and the computational domain on the right. The axisymmetric geometry of the round jet allows for two-dimensional simulations to be employed. Note that the effects of modeling the square-shaped turbulent mixing tunnel boundary as a circular one are assumed small due to its large distance from the jet region, and are ignored. The computational domain is 26.4 cm wide in the radial (x or 1 in the simulation) direction and 52.8 cm long in the axial (y or 2 in the simulation) direction. In terms of the nozzle diameter $d_0 = 1.1$ cm, it is $24d_0$ by $48d_0$. The domain size is identical to that used in the previous study because the starting point for current work is the input deck used by Cline [9]. The coordinate origin is located at the bottom left corner of the domain. The nozzle exit is positioned at the bottom left, with the jet axis aligned with the left boundary. Flow direction is from bottom to top. Mean velocity components are denoted U and V in the radial and axial directions, respectively.

2.2 Boundary Conditions

In xRAGE, the reflecting boundary condition and the periodic boundary condition are available for use. For a jet flow simulation, however, inflow and outflow boundary conditions are needed, and the 'freeze boundary' condition [10, p. 13] is used to emulate them. In the freeze boundary condition subroutine, all flow quantities (e.g., mass, momentum, energy, pressure, etc.) within the user-specified freeze regions are saved at the beginning of each timestep and restored at the end of each timestep. In between, the usual time integration is carried out, but the inflow and outflow boundary conditions

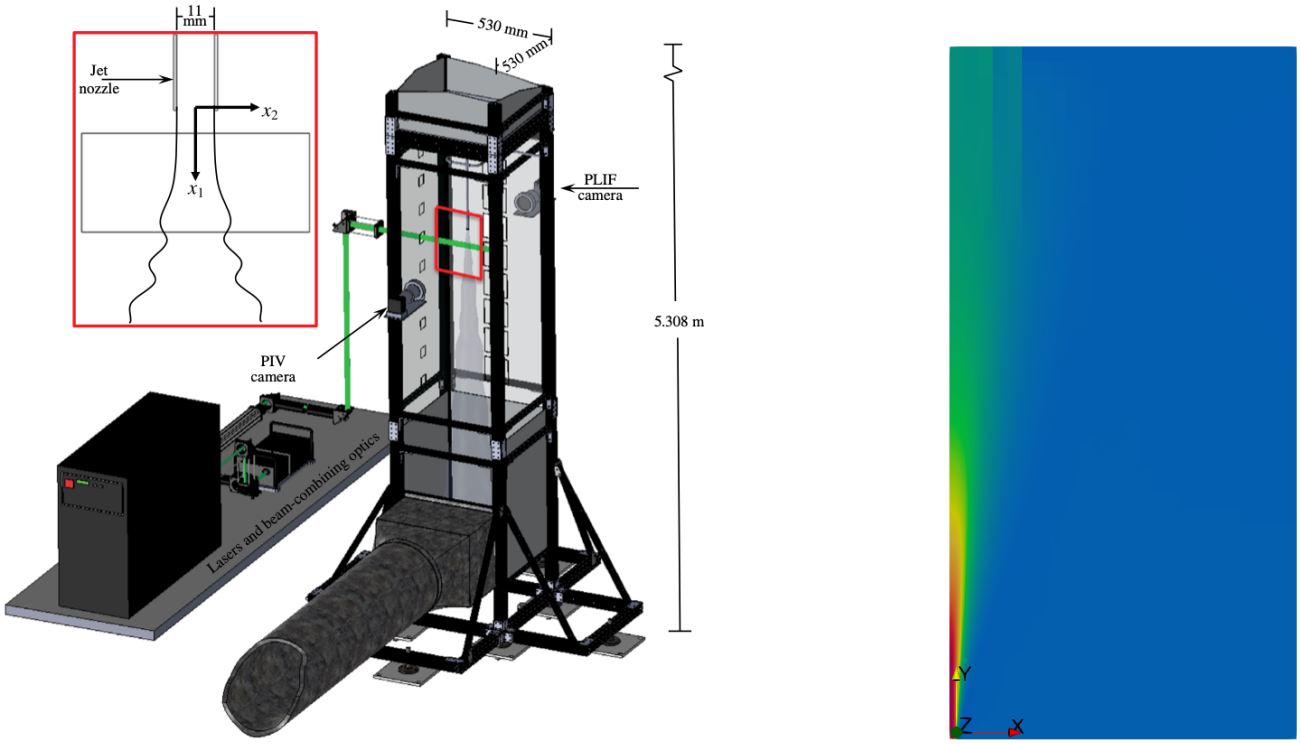

(a) (b)

Figure 1: (a) Rendering of experimental setup of turbulent mixing tunnel from Charonko and Prestridge [5]; (b) Computational domain in xRAGE simulations. The position and the extent of the jet flow are shown via the contours of the mean axial velocity (V). The coordinate origin $(0, 0)$ is located at the bottom left corner. The domain is 24- and 48-nozzle-diameter long in the radial (x) and axial (y) directions, respectively.

are not enfored. If a freeze region is specified as an outflow region, the flow quantities in the cells upstream of the freeze cells are saved instead, and restored in the freeze cells.

2.2.1 Inlet

The inlet mean velocities in the simulation are obtained by interpolating the experimental data [5] onto the computational mesh. The experimental data are available starting from $0.35d_0$ downstream of the nozzle exit, but those at $0.48d_0$ were used because data near the boundary of the measurement window may not be accurate. Figure 2 shows the radial profile of the mean axial velocity V. Mixing of the nozzle flow and the coflow is seen in the experimental data (red triangle symbols) in the region $x/d_0 = 0.5 - 0.55$. Since the simulation inlet condition is imposed at the nozzle exit, a polynomial curve (blue solid line) is fitted to the experimental data for $x/d_0 = 0 - 0.5$, but with $V = 0$ imposed at the nozzle wall, $x/d_0 = 0.5$. Blue square symbols denote velocities at centers of computational cells. The nozzle wall thickness in the experiment is 0.085 cm, but 0.103125 cm is used in the simulation so that it is an integer multiple of the smallest cell size 0.034375 cm. The treatment of the nozzle wall is the same as that of Cline [9], where zero velocites are specified within the nozzle wall. Note that the flow fields obtained from a few simulations without the nozzle wall were similar to those with the wall. The coflow velocity outside of the nozzle is constant at 66.34 cm/s, obtained from the experimental data. The material concentration at the inlet takes the top-hat shape, with the concentrations of (SF_6, air) being $(1, 0)$ inside of the nozzle and $(0, 1)$ otherwise.

2.2.2 Side Wall

Similar to the previous studies [8, 9], a dirichlet boundary condition is used at the side wall where $V = V_{coflow}$ and $U = 0$. Cline [8] initially used the reflecting boundary condition, but found that it produced reverse coflows along the side wall. The dirichlet boundary condition is enforced in the simulation by employing the xRAGE freeze boundary condition.

2.2.3 Outlet

At the outlet, a freeze region is specified in conjuction with the outflow designation. This enforces the flow quantities in the cells immediately upstream of the freeze cells are saved at the beginning of the current timestep (before the time

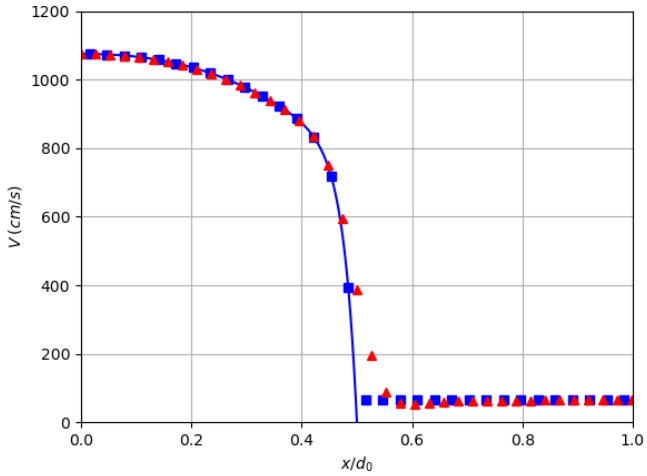

Figure 2: Inlet mean axial velocity V as a function of radial coordinate x scaled by the nozzle diameter d_0. Red triangles denote the experimental data. Blue solid line is a polynomial fit to the experimental data inside of the nozzle, but with an imposed zero velocity at the nozzle wall, $x/d_0 = 0.5$. Inside of the nozzle, $x/d_0 \leq 0.5$, blue squares denote velocities from the polynomial fit, but at discrete computational cell centers. Outside of the nozzle, the coflow velocity is constant.

integration), and restored in the freeze cells at the end of the current timestep (after the time integration).

2.3 Mesh

All previous studies [6, 8, 9] employed the adaptive mesh refinement (AMR) feature in xRAGE in order to reduce the simulation size, and therefore the computation time. Throughout the simulation, an AMR mesh changes dynamically with the flow, based on certain criteria involving gradients of, for example, density. In Cline [8, 9], six levels of mesh refinements were used with the minimum mesh size of 0.034375 cm (or $0.03125d_0$) and the maximum of 1.1 cm (or $1d_0$). The AMR mesh at the end of the simulation, $t = 1$ second, is shown in Figure 3(a). Shapes of mesh clusters resemble that of a spreading jet flow, and higher mesh levels (finer mesh sizes) are concentrated near the nozzle exit where gradients of flow quantities are steeper.

In the current study, a non-AMR static mesh, which is fixed throughout the entire duration of the simulation, is used. The main motivation is to reduce sources of simulation uncertainties so that any discrepancies between simulation and experimental results can be attributed to the turbulence model used in the simulation. Typical RANS simulations, such as those in this study, evolve from an initial, possibly unphysical flow fields, and eventually converge to a steady state. How the AMR mesh affects this evolving flow fields is not currently well understood by the author. Additionally, different mesh refinement criteria can potentially result in nonidentical flow fields, which will warrant further analyses of the AMR parameters. Another motivation is concenred with the grid refinement studies where coarser and/or finer grids are used to verify the convergence of simulation results. With the AMR mesh, interpreting the results of grid refinement studies may not be as straightforward because the mesh topology and spatial distribution can change when coarser/finer meshes are used, which again necessitates further analyses. For example, Israel [6] found that three grids of different resolutions did not lead to a converged solution despite the finest grid having a minimum mesh size of 0.016 cm; trying to diagnose such an issue would be easier if the parametric space of factors affecting the solution is smaller.

An example static mesh used in the study is shown in Figure 3(b). It employs the same number of levels of mesh refinement as well as the same minimum and maximum mesh sizes as the AMR mesh [8, 9]. By comparing the regions of the same mesh levels between the AMR and the static mesh in Figure 3, it can be seen that the static mesh has finer resolutions further away from the nozzle exit in both axial and radial directions. The static mesh will also alow mesh refinement studies to be conducted while maintaining the same mesh topology and distribution. It is worth mentioning that, for the two meshes shown in Figure 3, the static mesh, whose total number of grid cells is 2.85 times larger than that of the AMR mesh (112648 vs. 39508), reduced the simulation time by 37 percent (31 vs. 49 wallclock hours). The difference in computation speed may be due to the computational overhead associated with the AMR algorithm.

2.4 Turbulence Initial Conditions

The BHR turbulence models require initial values for turbulent kinetic energy (TKE) and turbulent length scale. Figure 4 shows the radial profile of turbulent kinetic energy from the experiment [5] at $0.48d_0$ downstream of the nozzle exit. The

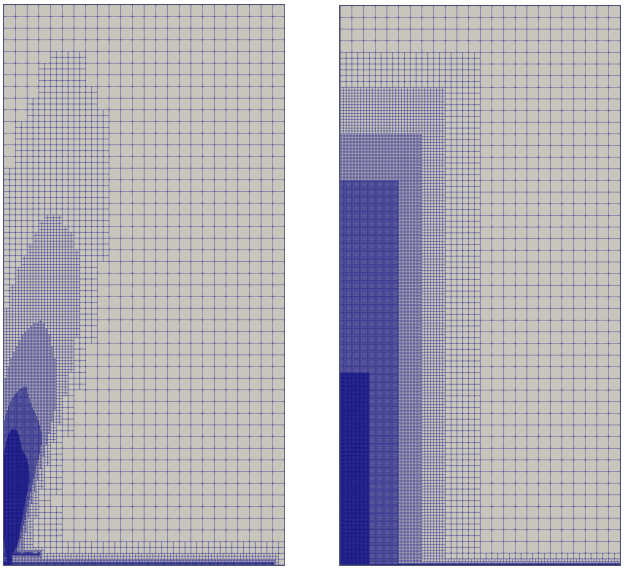

(a) (b)

Figure 3: Computational mesh: (a) AMR mesh at the end of the simulation $t = 1$ second; (b) Non-AMR static mesh. Both meshes have six levels of mesh refinement and the same minimum (0.034375 cm) and maximum (1.1 cm) mesh sizes.

TKE level peaks at approximately 10400 cm^2/s^2 in the turbulent shear layer close to the nozzle wall (although not likely to be accurate because of insufficient spatial measurement resolution), and decrease to approximately 1300 cm^2/s^2 in the nozzle center and 46 cm^2/s^2 in the coflow. Although xRAGE allows a user to assign different initial values for different materials, it does not allow specifying spatially varying initial values. Previous studies [8, 9] used the initial TKE's of 1700 cm^2/s^2 inside of the nozzle (SF_6) and 17 cm^2/s^2 everywhere else (air), and the initial turbulent length scales of 0.1 cm everywhere. The current study uses the same values as a starting point. Note that, because the freeze boundary condition is used at the inlet, the initial values are essentially the boundary conditions at the nozzle and coflow inlet, thereby rendering the choice of turbulence initial conditions possibly more important.

3 Examination of Computational Parameters

This section presents results concerning the effects of various computational parameters on the simulation results. These studies were carried out using the BHR 2 turbulence model because of shoter computation time and robustness. The BHR 3.1 model required smaller timestep sizes to suppress numerical instabilities. It can be reasonably assumed that the conclusions drawn from the BHR 2 studies will also apply to the BHR 3.1 results.

3.1 Steady State Convergence

Shown in Figure 5 are the time evolution of several flow variables (pressure, mass fraction of SF_6, and TKE) at seven probe locations dispersed throughout the computational domain. All quantities shown here (and many others not shown in the figure) level out by approximately 0.6 second, and therefore the simulation duration of one second is considered sufficiently long for the flow to reach a steady state. All simulations in this report are carried out up to one second, and the results presented are steady-state solutions at $t = 1$ second.

3.2 Boundary Conditions

3.2.1 Side Wall

When the dirichlet boundary condition $V = V_{coflow}$, $U = 0$ is imposed at the side wall, an abrupt jump in the mean velocities was observed near the side wall, as depicted in Figure 6. This issue may be addressed by expanding the computational domain in the radial direction, thus allowing the coflow more room to relax toward the imposed boundary condition. However, this is not possible because the radial domain boundaries are physically constrained by the wind tunnel walls. Note that the previously observed reverse coflows along the side wall [8] were not detected here. Another simulation was run with the reflecting boundary condition at the side wall, where V is allowed to slip and $U = 0$, while all other simulation parameters were kept the same. Its results are shown in Figure 7.

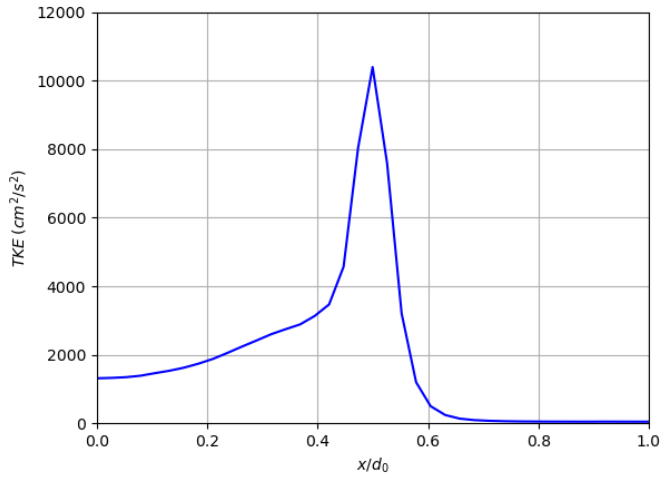

Figure 4: Turbulent kinetic energy as a function of the radial coordinate scaled by the nozzle diameter, obtained from the experimental data at $0.48d_0$ downstream of the nozzle exit.

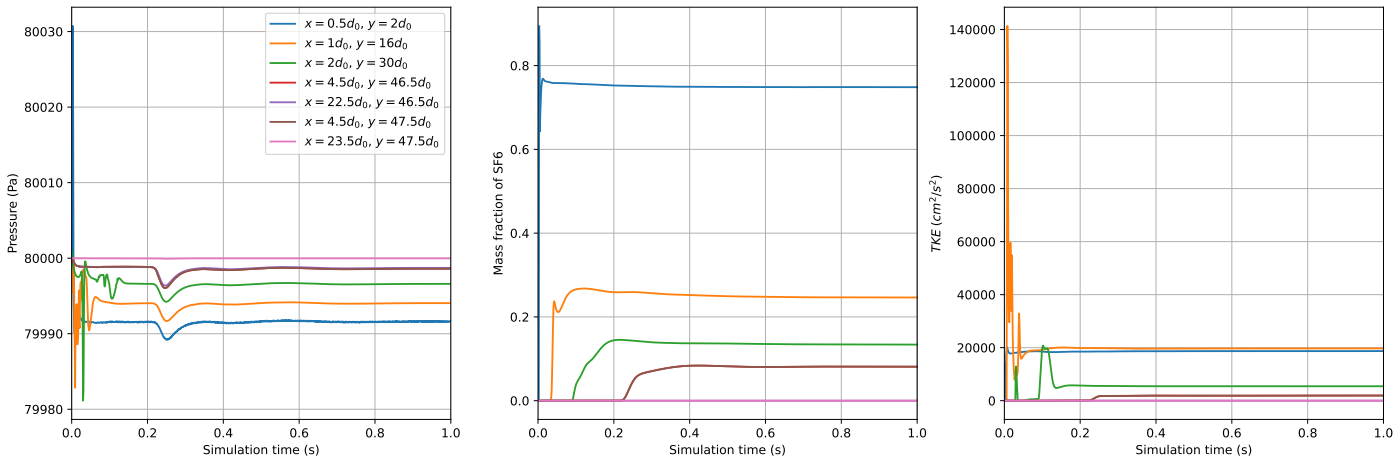

Figure 5: Time evolution of pressure (left), mass fraction of SF_6 (middle) and TKE (right) at seven probe locations. The coordinates of the probe locations are shown in the legend.

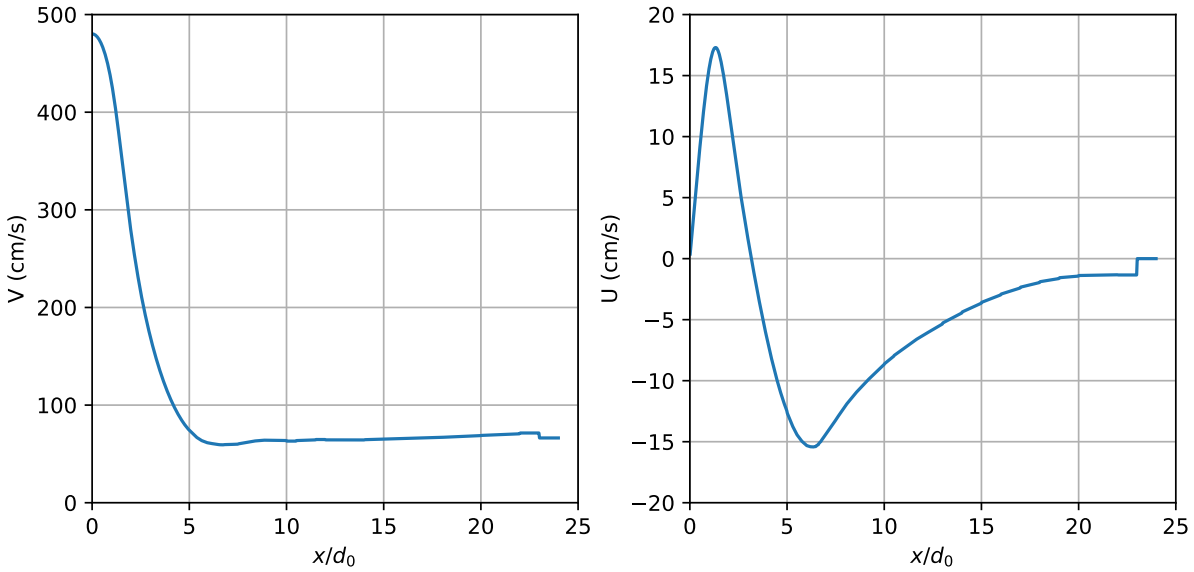

Figure 6: Mean axial (left) and radial (right) velocities at $16d_0$ downstream of the nozzle exit as a function of the radial coordinate scaled by the nozzle diameter d_0. Dirichelet boundary condition $V = V_{coflow}$ and $U = 0$ is used at the side wall.

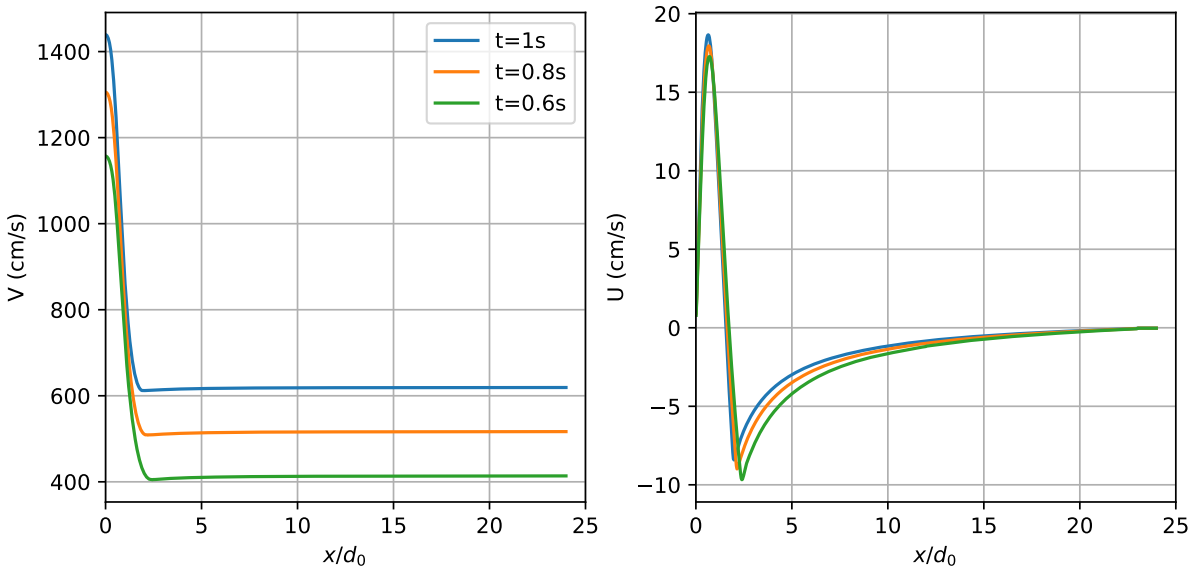

Figure 7: Mean axial (left) and radial (right) velocities at $16d_0$ downstream of the nozzle exit as a function of the radial coordinate scaled by the nozzle diameter d_0. Reflecting boundary condition is used at the side wall where V is allowed to slip and $U = 0$. Results are shown at simulation times 0.6, 0.8 and 1 seconds.

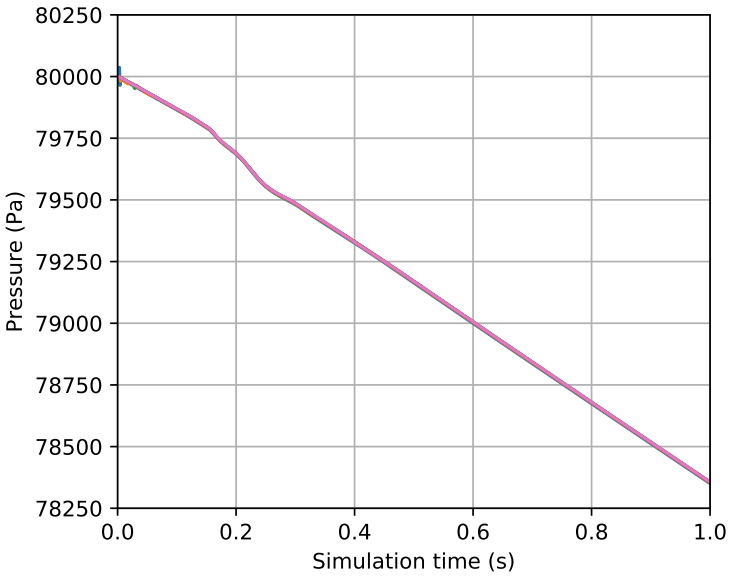

Figure 8: Pressure time traces at seven probe locations in the computational domain indicate a continuous pressure drop for the entire duration of the simulation. The probe locations are the same as those noted in Figure 5.

With the reflecting boundary condition, the mean velocities are seen to vary smoothly all the way to the side wall ($x/d_0 = 24$) and the abrupt jumps observed in Figure 6 do not appear. However, the magnitudes of V (left plot) are much larger than physical values. In fact, comparing the V curves at three different times 0.6, 0.8 and 1 seconds indicates that this dircrepancy becomes worse as the simulation progresses. The reason for this flow acceleration is a drop in the mean pressure everywhere in the computational domain except at the inlet where the pressure is fixed by the freeze boundary condition. Figure 8 shows this continuous pressure drop traced by the seven probes in the domain. It appears that the simulations with the dirichlet boundary condition circumvents the pressure drop by overly constraining the flow.

3.2.2 Modification of Inlet and Outlet Freeze Boundary Conditions

One motivation to make changes to the inlet and outlet freeze boundary conditions was to be able to use the reflecting boundary condition at the side wall because a comparison of the velocity profiles shown in Figures 6 and 7 seemed to suggest that the jet width may be reduced by doing so. Cline [9] showed the jet spreading faster in the simulation than in the experiment, and the hope was that this discrepancy may at least be partially resolved by imposing the reflecting boundary condition at the side wall. Another motivation was that the freeze boundary condition, which specifies the values of all flow quantities at the inlet and outlet, is not adequate for compressible flows; see, for example, Poinsot and Lele [11] and the references cited therein.

Following Grinstein [12], the pressure at the inlet is allowed to float, while the mass and momentum are specified. The internal energy follows from an equation of state. Note that, since the these modifications are made in the framework of the freeze boundary condition, we do not deal with the ghost cells, which are associated with true boundary conditions. The subscripts '1', '2' and '0' denote freeze cells (first internal cells), cells immediately downstream of the freeze cells (second internal cells), and specified values, respectively. The superscripts 'n' and 'n-1' denote the current and previous timestep, respectively. The following was implemented in the freeze boundary condition subroutine.

$$\begin{aligned} \rho_1 &= \rho_0, \\ v_1 &= v_0, \\ u_1 &= 0, \\ p_1^n &= p_2^{n-1}, \\ e_1 &= e(\rho_1, p_1). \end{aligned} \tag{1}$$

At the outlet boundary, the approach described by Grinstein [13] is implemented within the freeze boundary condition subroutine. The subscripts 'N' and 'N-1' denote freeze cells (last internal cells) and cell immediately upstream of the freeze cells (second last internal cells), respectively. As before, the superscripts 'n' and 'n-1' denote the current and previous timestep, respectively.

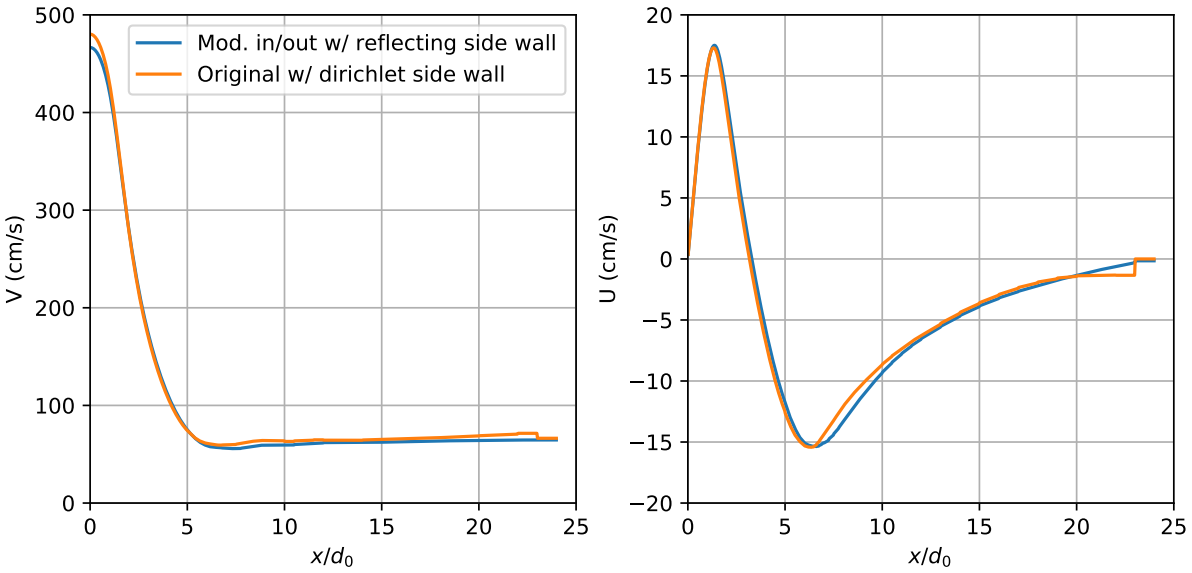

Figure 9: Mean axial (left) and radial (right) velocities at $16d_0$ downstream of the nozzle exit as a function of radial coordinate scaled by the nozzle diameter d_0. Blue curve is obtained with the modified inlet/outlet freeze boundary conditions, equations (1) and (2), and with the reflecting boundary condition at the side wall. Orange curve is obtained without the inlet/outlet modifications, and with the dirichlet boundary condition at the side wall.

$$Q_N^n = (1-\epsilon)Q_N^{n-1} + \epsilon Q_{N-1}^{n-1}, \tag{2}$$

where

$$\epsilon = v_{N-1}^{n-1}\Delta t/\Delta x_{out}, \tag{3}$$

Δt is the integration timestep, and Δx_{out} is the grid spacing at the outflow boundary. The mass and momentum densities in the freeze cells are determined by equations (2) and (3). The pressure in the freeze cells is determined by $p_N^n = (1-\gamma)p_{amb} + \gamma p_{N-1}^{n-1}$, where $\gamma = r_{N-1}/r_N$; p_{amb} is the inlet pressure, r_{N-1} and r_N are the distances from the inlet to the $(N-1)$th and Nth cell centers, respectively. The internal energy is computed from an equation of state $e = e(\rho, p)$. For details, please refer to the xRAGE branch `mji_jet`.

Figure 9 shows the mean velocities from a simulation with the above inlet/outlet modifications, and with the reflecting boundary condition at the side wall. It can be seen that the mean velocities vary smoothly all the way to the side wall without any jumps near the wall. The results are surprisingly similar to those of the simulation without the inlet/outlet modifications, and with the dirichlet boundary condition at the side wall. The jet width is not much affected by the modifications.

Figure 10 shows the mean pressure measured by the seven probes disperesed througout the computational domain. Unlike those seen in Figure 8, the mean pressure traces do not continuously drop, although periodic oscillations of small magnitudes are observed. This will be further investigated in the next section through mesh studies. From here on, all results presented are obtained with the modified inlet and outlet freeze boundary conditions.

3.3 Mesh

Figure 11 shows five different meshes used to study mesh effects on the flow, and Table 1 summarizes them in detail. The finest mesh spacing Δx_{min} is identical for all, but the extent of the region with the smallest mesh size (see the last column in Table 1), the largest mesh spacing Δx_{max}, and the number of mesh refinement levels vary. This approach can be regarded as a mesh refinement study where mesh is refined in all flow regions except where the mesh size is Δx_{min}. For example, mesh06 halves mesh sizes of mesh03 everywhere in the domain except in the region $(2.5d_0, 16.5d_0)$. Similarly, mesh08 halves mesh spacings of mesh05 everywhere except in the region $(2.5d_0, 16.5d_0)$. Comparing mesh03 and mesh05, the latter halves the coarsest mesh spacing of the former, while keeping all other mesh sizes the same. Similarly, mesh08 halves only the coarsest mesh spacing of mesh06. Lastly, mesh07 employs the finest mesh covering a large portion of the domain, $(14d_0, 41d_0)$, and therefore its total number of cells is almost eight times larger than that of mesh03. Note that, if an AMR mesh was used, a systematic mesh study like this would be difficult because the user only gets to specify Δx_{max} and the number of mesh refinement levels, while the AMR algorithm determines the mesh distribution and topology.

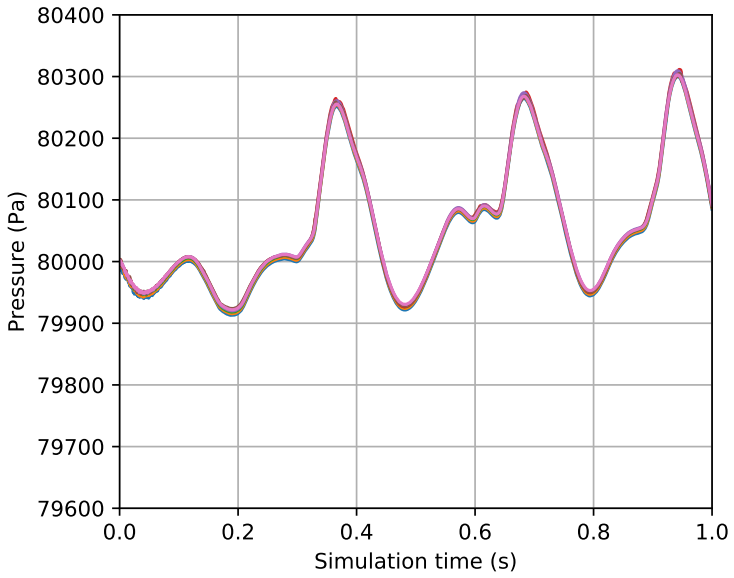

Figure 10: Pressure traces at the seven probe locations in the computational domain. Results are obtained with the modified inlet/outlet freeze boundary conditions, and with the reflective boundary condition at the side wall. Unlike those in Figure 8, pressure does not continuously drop, although oscillations are observed.

A typical mesh refinement study where the mesh spacing is refined in the entire domain would halve Δx_{min} as well, and this would lead to halving the simulation timestep size (if the CFL number is kept the same). This type of study would be useful, but left as a future task because of two reasons: one is the associated large computational cost and time, and the other is that the current smallest mesh size of 0.034375 cm is deemed adequate based on previous RANS and LES studies of jet flows in the literature.

Table 1: Details of five meshes used to study the effects of mesh on simulation results.

Name	No. of cells	No. of levels	Δx_{max} (cm)	Δx_{min} (cm)	Δx_{min} region boundary $(x/d_0, y/d_0)$
mesh03	112648	6	1.1	0.034375	(2.5,16.5)
mesh05	113944	5	0.55	0.034375	(2.5,16.5)
mesh06	274032	5	0.55	0.034375	(5,33)
mesh07	876320	3	0.1375	0.034375	(14,41)
mesh08	279312	4	0.275	0.034375	(5,33)

Figure 12 shows the pressure traces in time from simulations with five different meshes. The probe is located at $(x/d_0, y/d_0) = (1, 16)$, but similar plots are also obtained for other probe locations not shown here. The pressure signals exhibit oscillations whose amplitude grows initially but decays later in time, although the simulation duration for mesh03 is not sufficiently long to display the decaying portion. For mesh05, mesh06 and mesh08, oscillations appear to damp out toward the end of the simulations. For mesh07, which employs the best mesh resolution, shows very small-amplitde oscillations all the way to the end of the simulation. Interestingly, the pressure magnitudes near the end of the simulations appear to decrease with Δx_{max}. Mesh07, which uses the smallest Δx_{max}, has the smallest pressure magnitude, followed by mesh08, then by both mesh05 and mesh06, which share the same Δx_{max}, and then by mesh03, which employs the largest Δx_{max}. This trend is counter to the author's initial guess that the opposite would be true because a larger Δx_{max} should accompany a larger numerical dissipation, which in turn reduces the spurious numerical wave reflections at the outlet, and leads to less contamination of the solution. The causes of neither the pressure oscillation nor the pressure magnitude are not clear, but no further analyses were carried out. Note that, at hundreds of pascals, both the oscillation amplitudes and the mean pressure magnitudes of these pressure signals are small.

Figure 13 plots radial profiles of V, U, TKE and b at $16d_0$ downstream of the nozzle exit. Despite having different pressure signals (Figure 12), all flow quantities shown here look very similar, indicating little effects of mesh on results, and therefore 'convergence' of the flow fields with mesh refinement. Based on the results presented in Figures 12 and 13, mesh05 will be used from here on because its pressure signal is well stabilized by the end of the simulation $t = 1$, and its total number of cells is small.

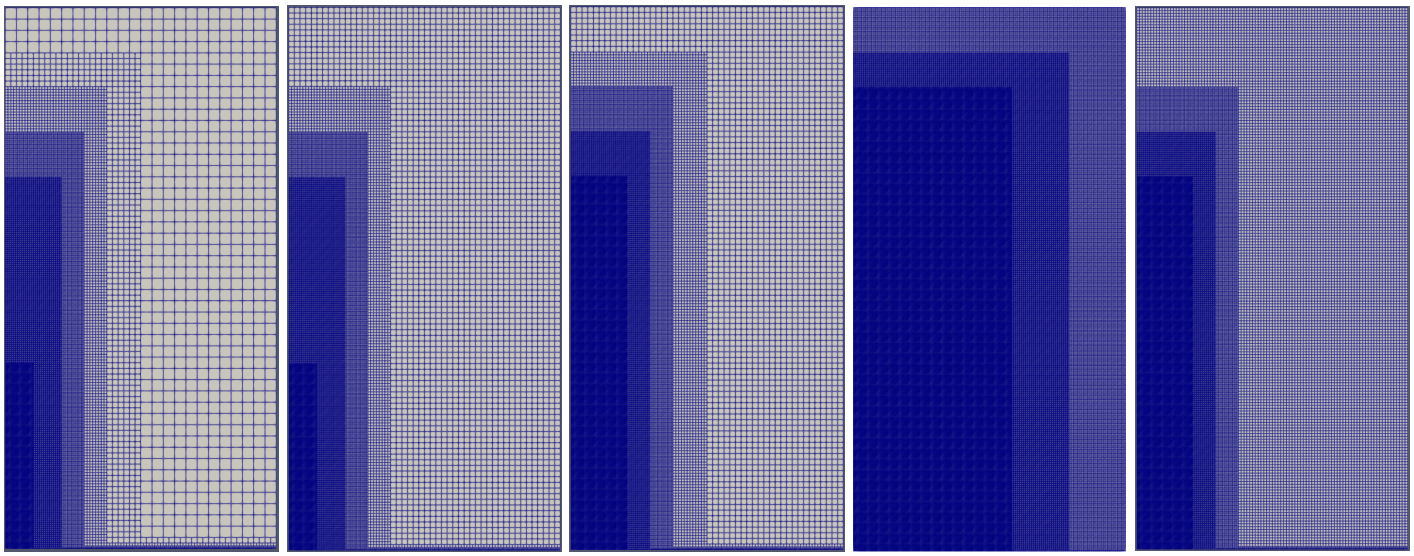

(a) (b) (c) (d) (e)

Figure 11: Five meshes used to study the effects of mesh on the flow: (a) mesh03; (b) mesh05; (c) mesh06; (d) mesh07; (e) mesh08. The finest mesh size Δx_{min} is kept the same for all, but the extent of the region with Δx_{min}, the coarsest mesh size Δx_{max}, and the number of mesh refinement levels vary. Refer to Table 1 for details.

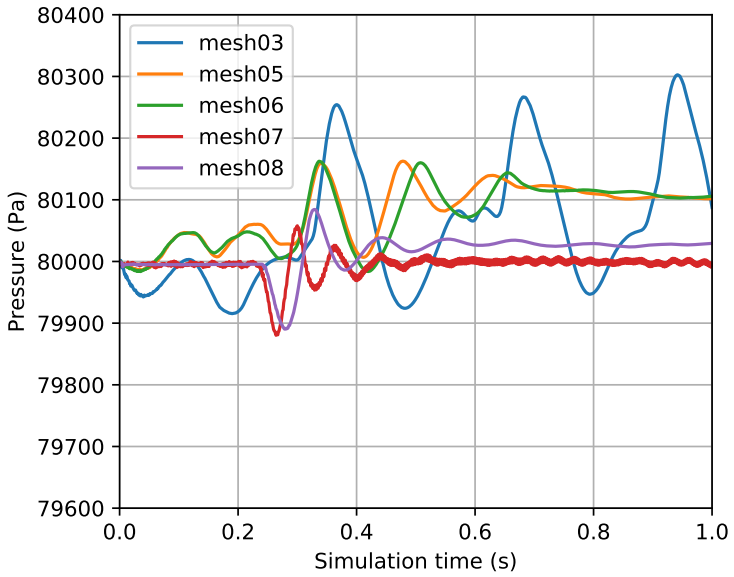

Figure 12: Pressure traces at the probe location $(x/d_0, y/d_0) = (1, 16)$ from simulations with five meshes shown in Figure 11 and described in Table 1. Other probe locations not shown here exhibit similar pressure traces.

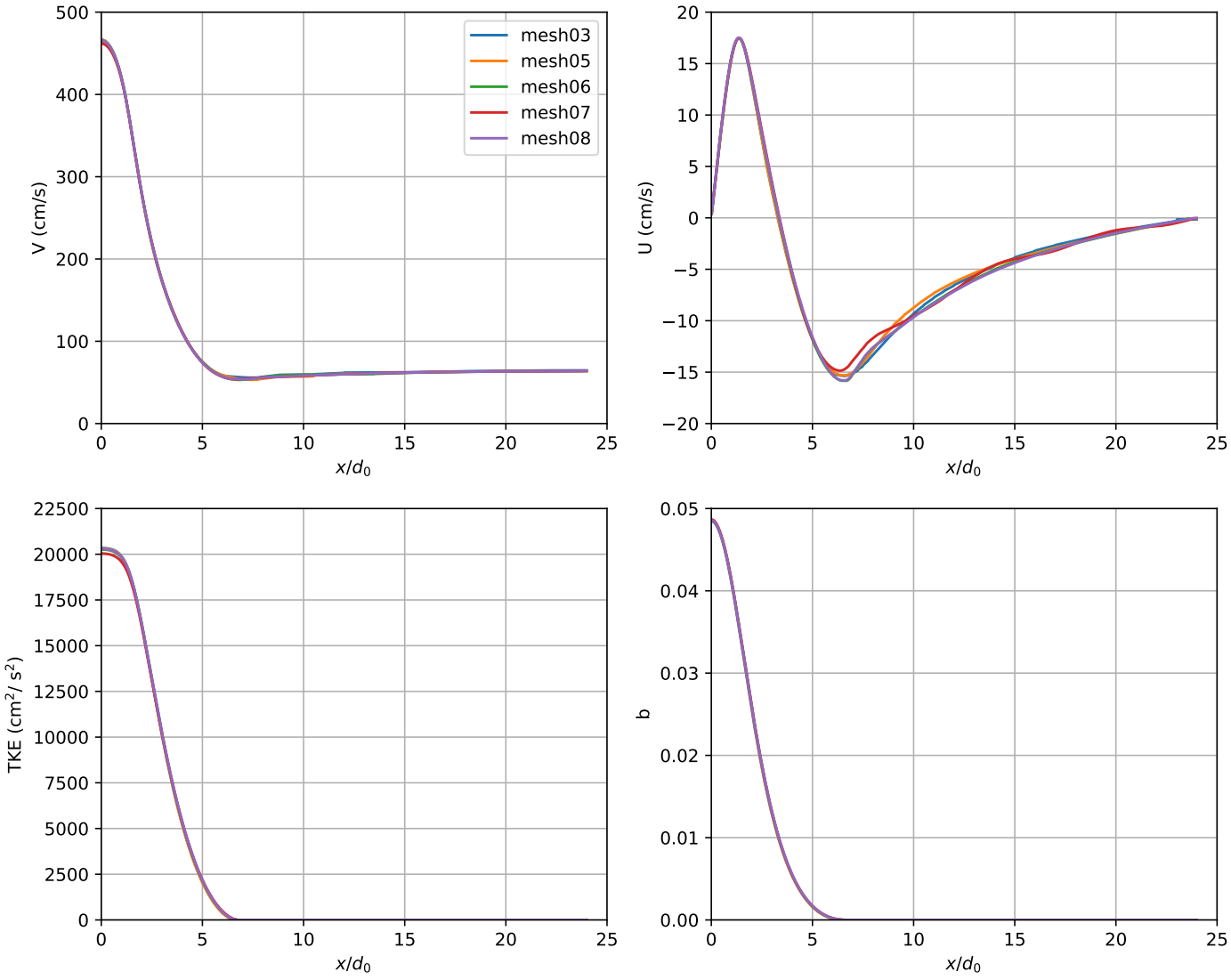

Figure 13: Radial profiles of flow variables V, U, TKE and b at $16d_0$ downstream of the nozzle exit from simulations with five different meshes shown in Figure 11 and described in Table 1.

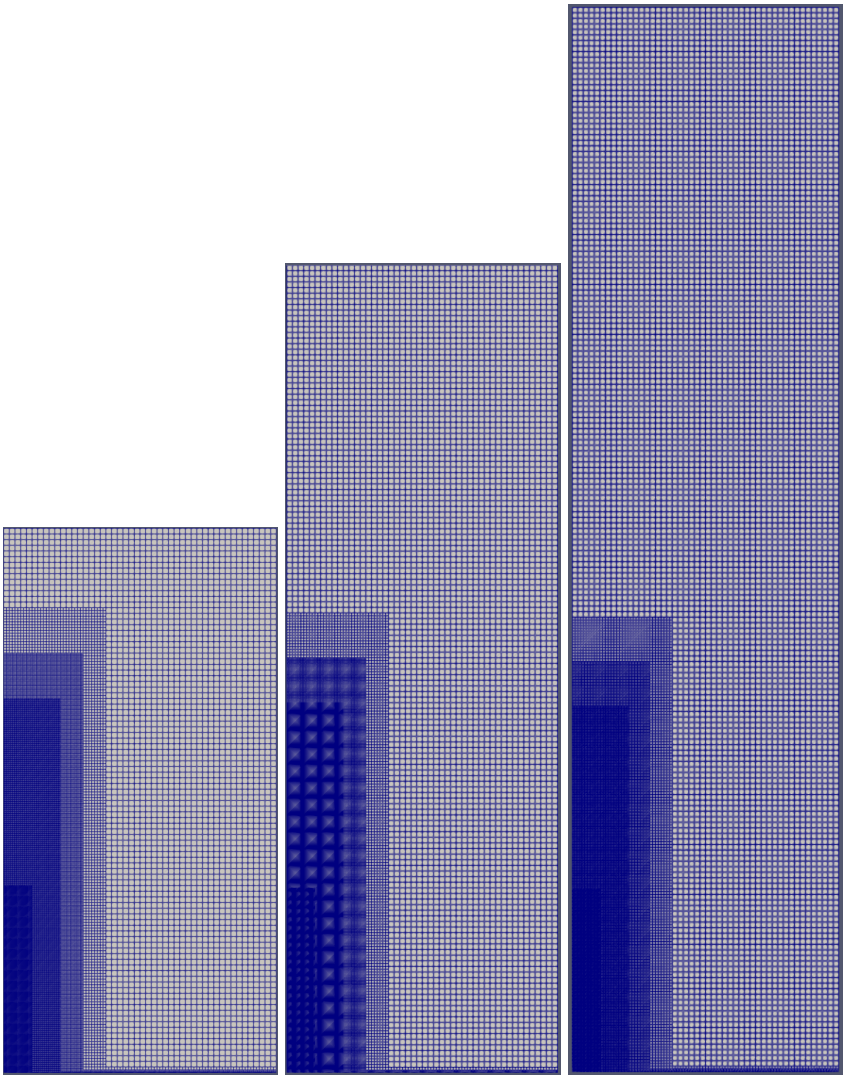

(a) (b) (c)

Figure 14: Three domain sizes used to study the effects of domain size on the flow: (a) mesh05; (b) mesh05_1p5d (1.5 times longer axial domain length); (c) mesh05_2p0d (2 times longer axial domain length).

3.4 Domain Size

For compressible flow simulations, domain boundaries that are not physical walls require special treatments to prevent wave reflections. They are: properly formulated boundary conditions based on characteristics (see, for example, [11]), and sponge layers. The author is not aware of any implementation of such treatments in xRAGE, which provided the reason for studying the effects of domain size. The idea is that, if the wave reflection at the outlet affect the flow fields significantly, simulations with the outlet positioned at different distances from the inlet may lead to different flow fields, either temporaly or spatially, since the reflected waves need to travel different distances.

Figure 14 shows the three domains used in the study. The domain length is fixed in the radial direction, and the axial length is varied: mesh05 has the original axial domain length of $48d_0$, mesh05_1p5d has a fifty percent-larger length of $72d_0$, and mesh05_2p0d a hundred percent-larger length of $96d_0$. All three share the identical mesh except for the added sections near the outlet which are filled with the coarsest mesh.

In Figure 15 the pressure traces in time are shown at the probe location $(x/d_0, y/d_0) = (1, 16)$. It is seen that larger domain sizes result in pressure oscillations of both larger amplitudes and longer periods, which therefore take longer to decay. The two larger-domain simulations were carried out until the simulation time $t = 3$ seconds. Addtionally, the pressure traces from the two larger-domain simulations seem to settle at the same pressure level of approximately 80300 pascals; this may indicate that the axial domain size should be at least $72d_0$ long. No further analyses were performed mainly because of the results shown in the next figure.

Figure 16 shows the radial profiles of flow variables V, U, TKE, and b from simulations with the three domain sizes. Although the two larger-domain simulations were integrated up to $t = 3$ seconds, the results shown here are obtained at

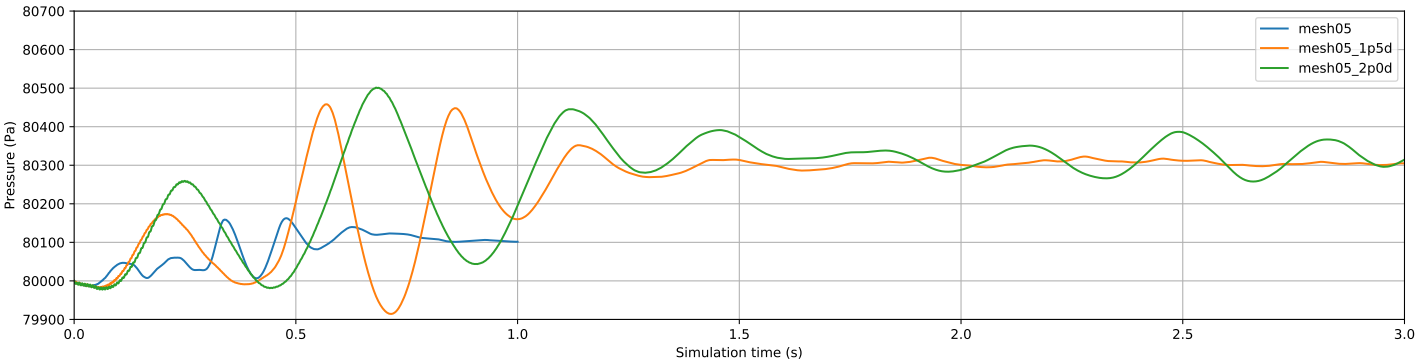

Figure 15: Pressure traces at the probe location $(x/d_0, y/d_0) = (1, 16)$ from simulations with the three different domains shown in Figure 14.

$t = 1$ second; at this time, the two larger-domain simulations are going through transients as indicated by the pressure traces in Figure 15. Comparisons of the flow variables indicate that there are no differences between simulations with different domain sizes. Based on this result, mesh05 with the axial length of $48d_0$ will be used from here on.

3.5 Timestep Size

The simulation timestep size is determined by the user-specified Courant-Friedrichs-Lewy (CFL) number, grid size, and the velocity fields according to

$$\Delta t = \text{CFL} \times \frac{\Delta x}{3(|V| + c)}, \tag{4}$$

where $|V|$ is the velocity magnitude and c is the sound speed.

Simulations were initially carried out with a CFL number of 0.9, but anomalous velocity fields were observed. This is seen from the blue curves in Figure 17, which plots radial profiles of V, U, TKE and b at $2d_0$ downstream of the nozzle exit. In the V plot (upper left), a region with negative velocities exists approximately from $1.3d_0$ to $2.1d_0$. In the U plot (upper right), velocities overshoot approximately from $2.7d_0$ to $6.5d_0$. This anomalous behavior is caused by a counterclockwise-rotating vortex located downstream of the nozzle exit and outward from the nozzle wall; see Figure 18a, which shows the contours of mean radial velocity U field at the CFL number of 0.9. As the CFL number is reduced from 0.9 to 0.5, the vortical structure disappears; see Figure 18b.

Initially, it was not clear what was causing the spurious vortical structure to appear. Different initial flow fields were tried without success based on the idea that it develops from unphysical initial fields and never gets completely 'washed away' as the simulation progresses. Original freeze boundary conditions were restored to see if the inlet/outlet modifications were causing it; they did not. It was found later that the cause lay with the mesh: AMR vs. non-AMR static mesh. This was perplexing because the static mesh had a better resolution in the region where the spurious vortical structure appeared. Stepping through the animations of the flow fields developing from an initial condition revealed that a similar vortical structure develops initially in the AMR mesh (with a CFL number of 0.9), but quickly gets dissipated by the coarser mesh spacing. How the AMR mesh is able to 'decide' not to resolve this structure and to stop refining in this region is not clear, but no further analyses were performed. As seen earlier, with the non-AMR static mesh, the spurious structure is removed only by reducing the timestep size.

As the CFL number is reduced from 0.9 to 0.5, 0.25 and 0.1, the radial profiles shown in Figure 17 appear to converge. At $16d_0$ (Figure 19) and $30d_0$ (Figure 20) downstream of the nozzle exit, similar convergences with the CFL number are observed. Note that the timestep size study was performed with mesh03, but minimal differences from mesh05 are expected.

3.6 BHR 3.1

Simulations with the BHR 3.1 model were performed with mesh05. Initially, a CFL number of 0.9 was used, but numerical instabilities emanating from a location of mesh transition prevented obtaining a meaningful solution. Reducing the CFL number to 0.5 stabilized the solution. Subsequently, the CFL number was further decreased to 0.25. As shown in Figure 21, the smaller CFL number of 0.25 only changes the results slightly from the CFL number of 0.5.

A close examination of the V plot (upper left) in Figure 21 reveals that the curves dip down very near the jet axis, $x/d_0 = 0$ for both CFL numbers. This dip is also observed, although not explicitly mentioned, in the previous study [9], which used an AMR mesh and did not modify the freeze boundary conditions at the inlet/outlet. Therefore, this dip seems

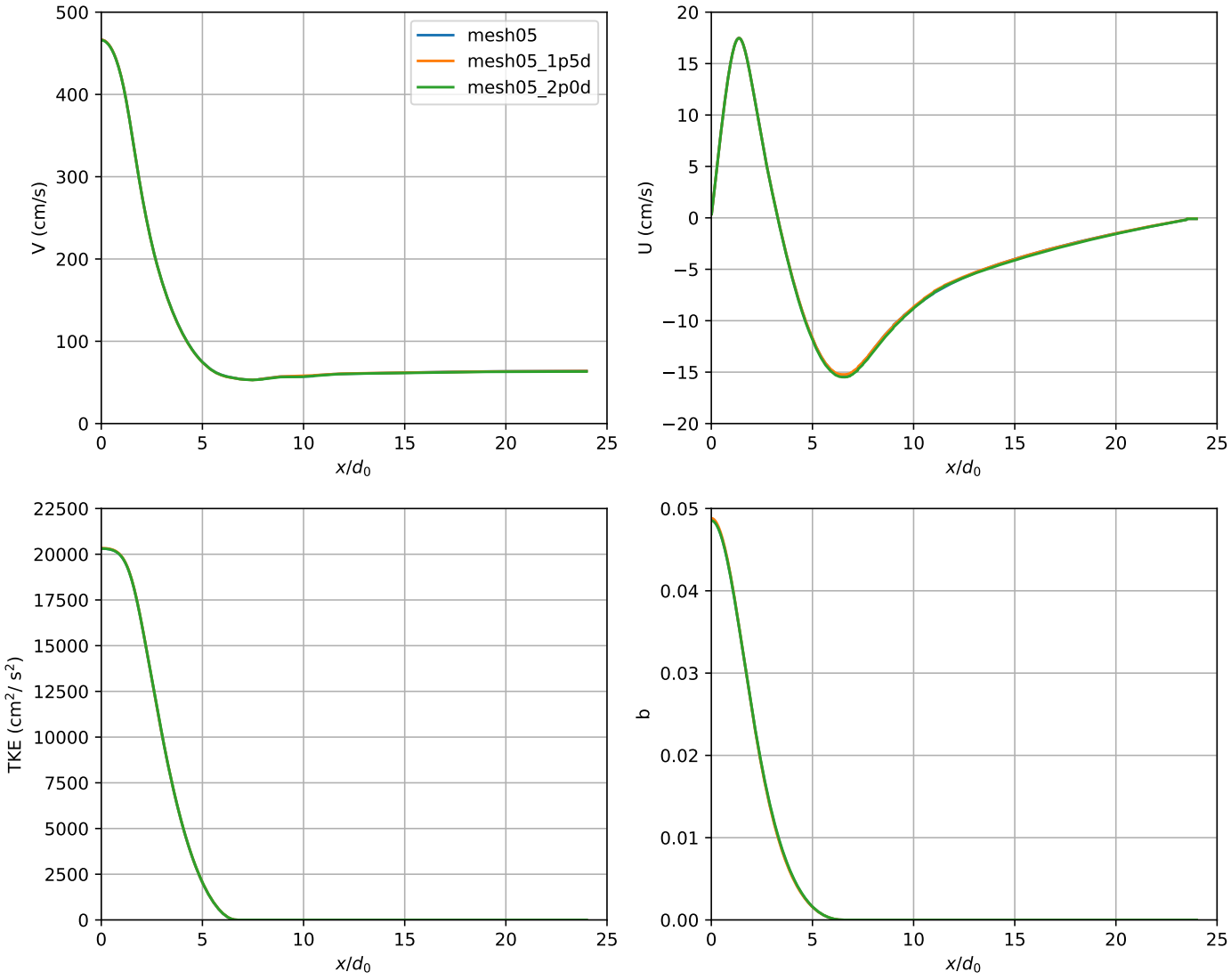

Figure 16: Radial profiles of flow variables V, U, TKE and b at $16d_0$ downstream of the nozzle exit from simulations with the three different domains shown in Figure 14.

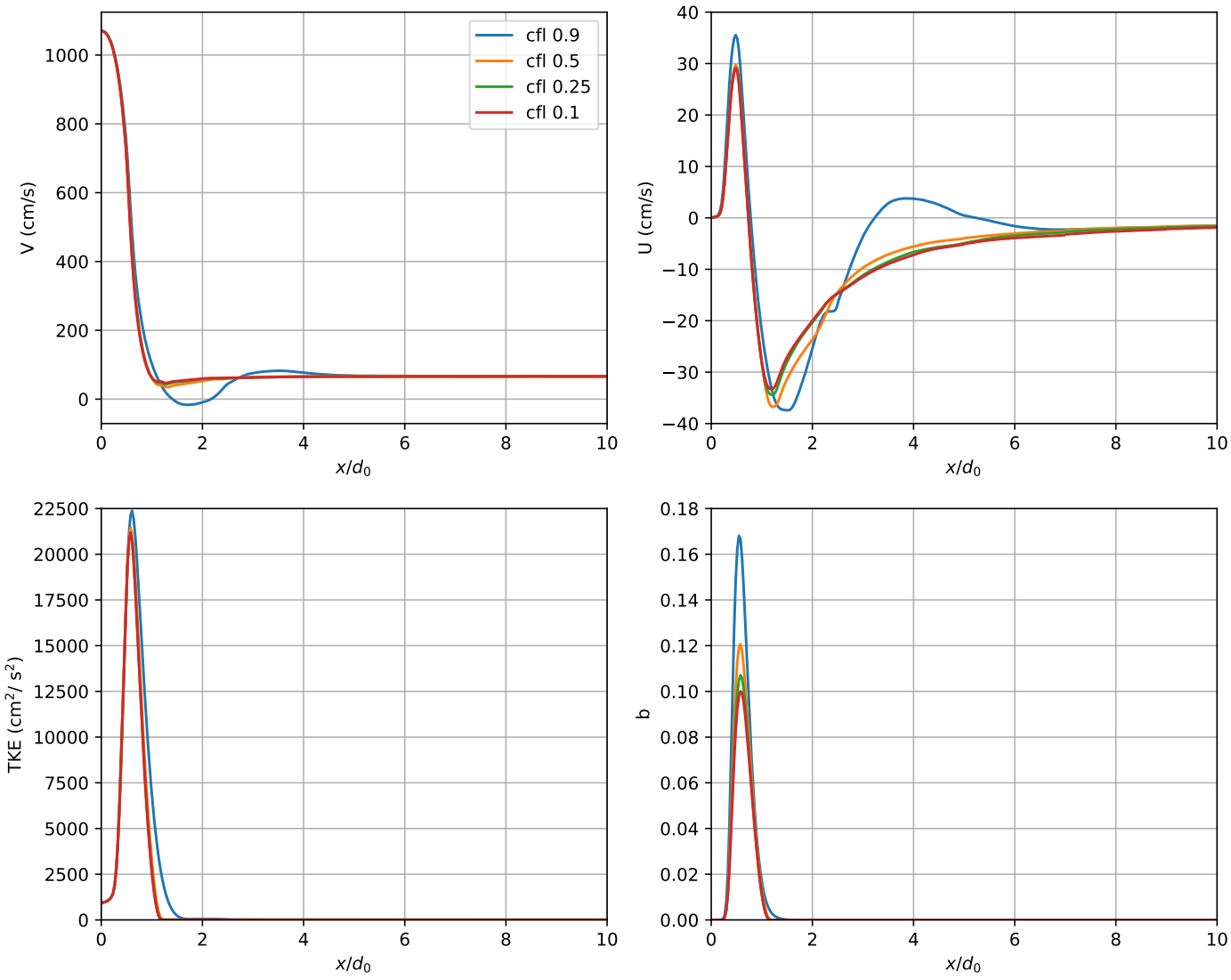

Figure 17: Radial profiles of flow variables V, U, TKE and b at $2d_0$ downstream of the nozzle exit from simulations with four different CFL numbers 0.9, 0.5, 0.25 and 0.1.

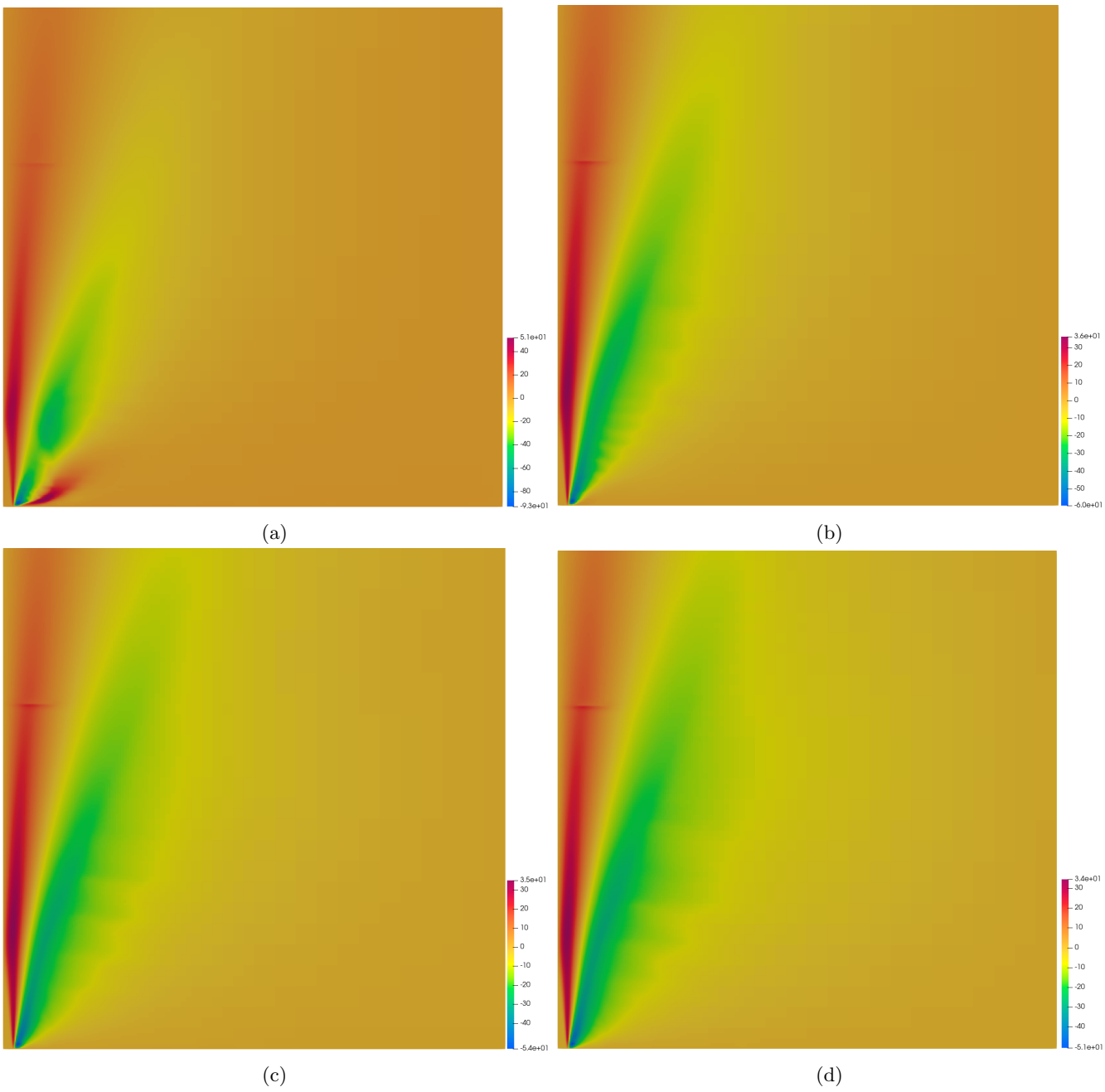

(a) (b)

(c) (d)

Figure 18: Mean radial velocity (U) field at four different CFL numbers: (a) 0.9; (b) 0.5; (c) 0.25; (d) 0.1. The field of view is approximately $24d_0$ wide and $24d_0$ high. The nozzle exit is positioned at the left end of the lower boundary. The lower and upper bounds of the contours in the four plots are (-93, 51), (-60, 36), (-54, 35) and (-51, 34), respectively.

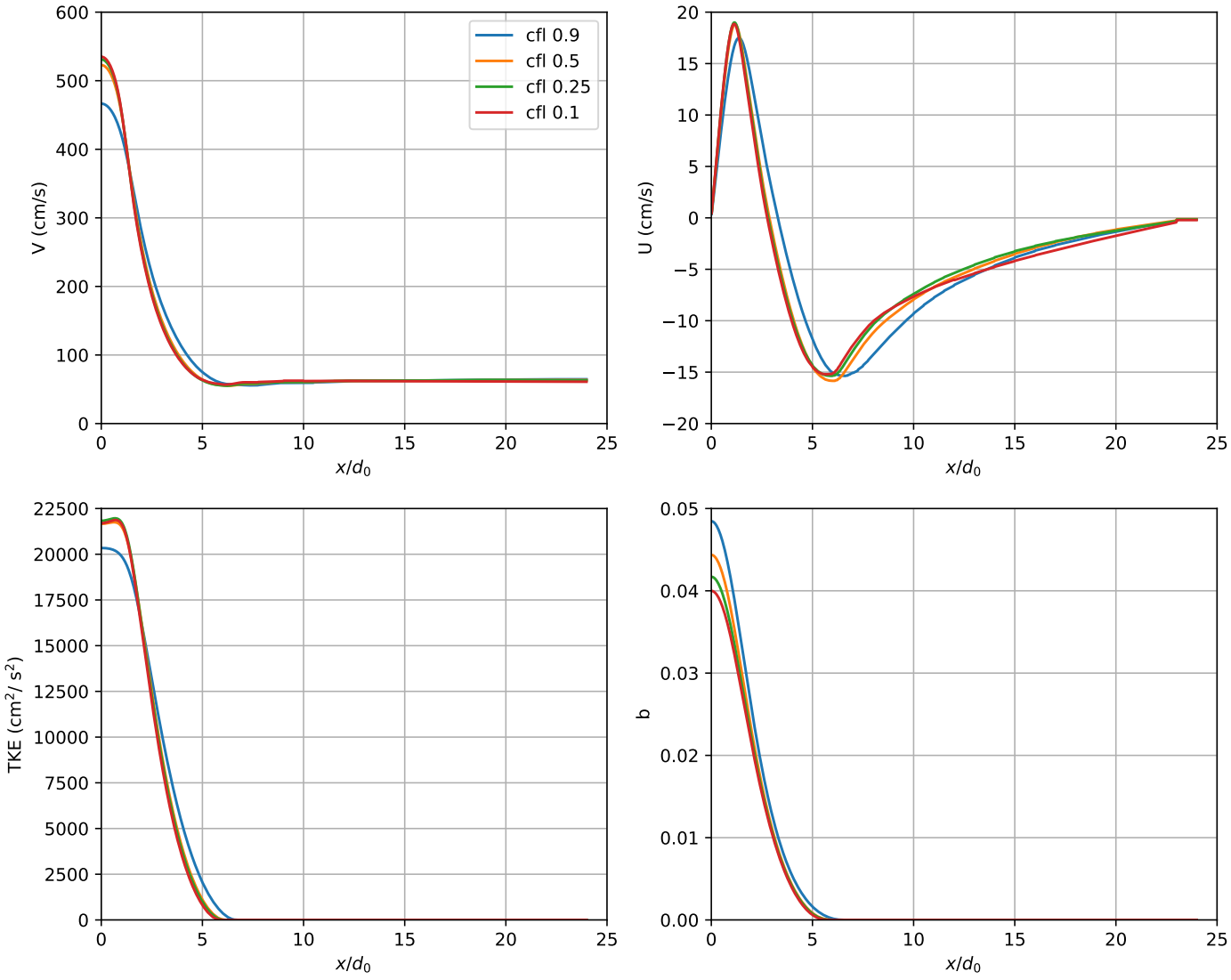

Figure 19: Radial profiles of flow variables V, U, TKE and b at $16d_0$ downstream of the nozzle exit from simulations with four different CFL numbers 0.9, 0.5, 0.25 and 0.1.

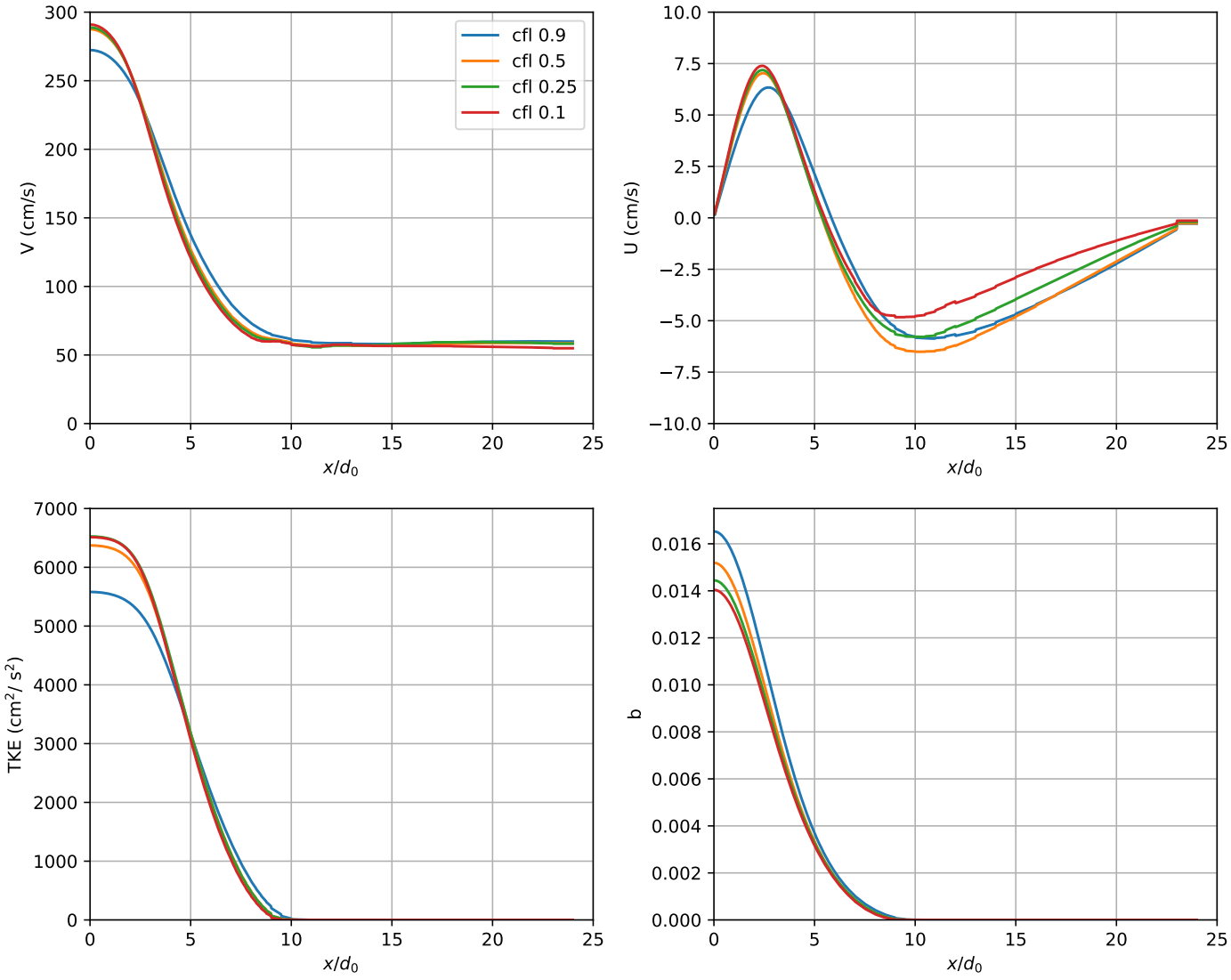

Figure 20: Radial profiles of flow variables V, U, TKE and b at $30d_0$ downstream of the nozzle exit from simulations with four different CFL numbers 0.9, 0.5, 0.25 and 0.1.

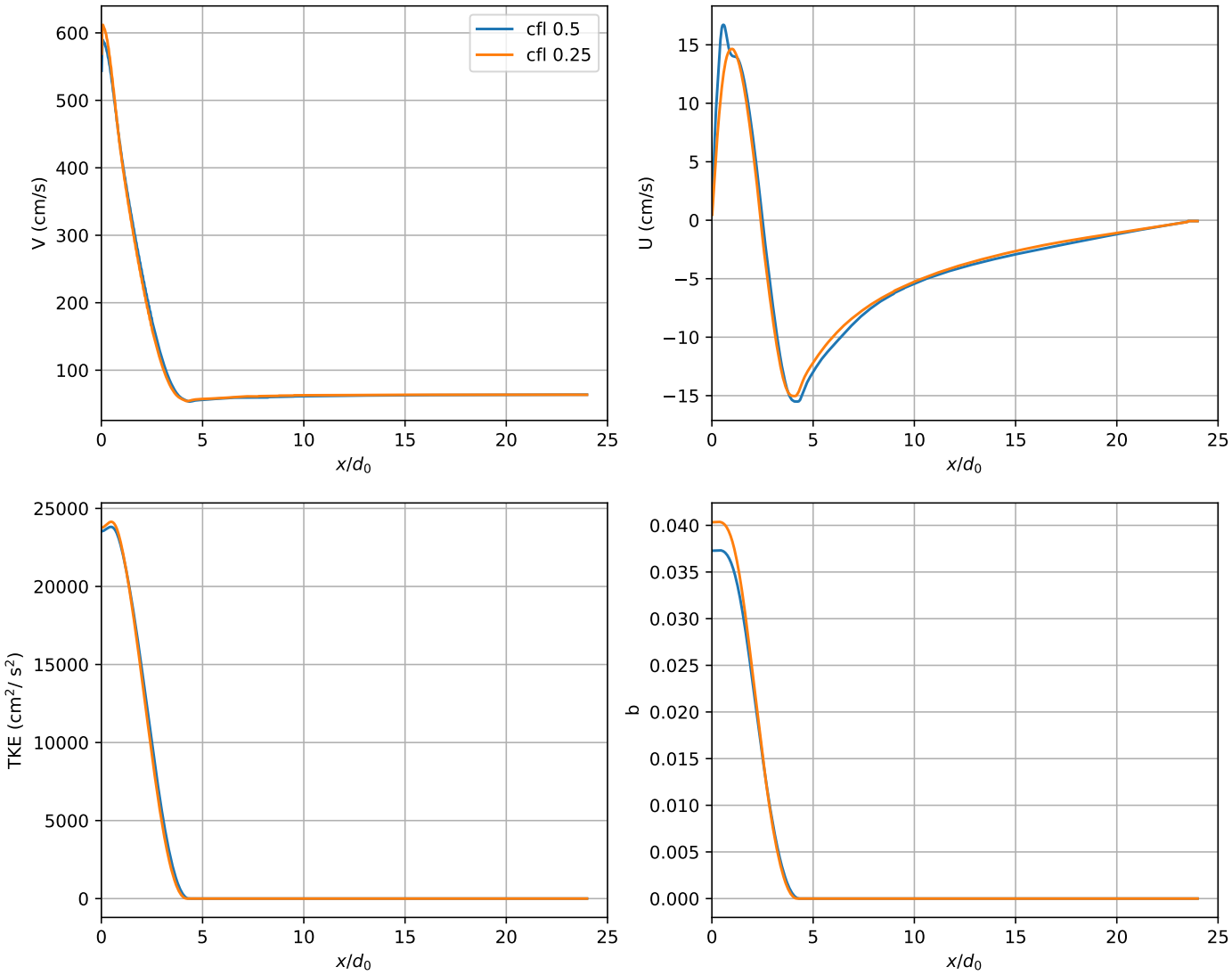

Figure 21: Radial profiles of flow variables V, U, TKE and b at $16d_0$ downstream of the nozzle exit from BHR 3.1 simulations with two different CFL numbers 0.5 and 0.25.

to be associated with the BHR 3.1 model in xRAGE. A comparison with results from a separate simulation of 2d planar jet (not shown here) indicates that it may specifically have to do with the axisymmetric geometry. Saenz and Rauenzahn [7] addressed the BHR axisymmetric boundary condition issue. In addition, the shear component of the Reynolds stresses, and the radial component of the mass flux (orange curves in the bottom two plots in Figures 22, 23, and 24) seem to indicate the correct bahavior at the jet axis. It is not clear at this time if the dip is indeed related to the BHR boundary condition or a manifestation of some other issues. This will be further investigated in the FY24.

4 Results

In this section, BHR 2 and 3.1 model results are compared with the experimental data [5]. All simulations were performed with mesh05 and a CFL number of 0.5. In addition, simulation results showing the the effets of the initial turbulent length scale on the flow fields are presented for both models. Note that in-depth analyses of these results were not carried out in the FY23 as the focus was on examining the effects of an array of computational parameters on simulation results. Detailed analyses of the results in this section will be performed in the FY24 as we try to understand the causes of discrepancies between the simulation and the experiment, and to consider ways to improve the model predictions. This will, for example, involve analyses of turbulence budgets. It may also involve analyses of the dissipation (or turbulence length scale) equation as it was indicated responsible for the overestimation of the spreading rate of a round jet [14].

4.1 Comparison of BHR 2 and 3.1 Model Predictions with Experimental Data

Initial TKE's used in these simulations are 1700 cm^2/s^2 for SF_6 and 17 cm^2/s^2 for air. An initial turbulent length scale of 0.1 cm is used everywhere. Figures 22, 23 and 24 show radial profiles of flow variables V, U, TKE and b at $2d_0$, $16d_0$ and $30d_0$ downstream of the nozzle exit, respectively. The following are a brief summary of observations. First, models predict the jet spreading faster than in the experiment, which is evident even at $2d_0$ downstream of the nozzle exit. Second, models predict much higher levels of turbulent quantities (TKE and b) than in the experiment, especially at $2d_0$. Third, the BHR 3.1 model predicts higher levels of turbulence quantities than the BHR 2 does, especially at $2d_0$.

4.2 Turbulent Length Scale Effect

Three different values 0.01 cm, 0.1 cm and 1.0 cm of the initial turbulent length scale S_0 are tested here.

4.2.1 BHR 2

Figures 25, 26 and 27 show radial profiles of flow variables V, U, TKE and b at $2d_0$, $16d_0$ and $30d_0$ downstream of the nozzle exit, respectively. Additionally, Figure 28 shows how the TKE profile changes from $2d_0$ to $16d_0$ to $30d_0$. Interpretation of these results is left for next year (FY24), which will focus more on the BHR turbulence models.

4.2.2 BHR 3.1

Figures 29, 30 and 31 show radial profiles of flow variables V, U, TKE and b at $2d_0$, $16d_0$ and $30d_0$ downstream of the nozzle exit, respectively. Additionally, Figure 32 shows how the TKE profile changes from $2d_0$ to $16d_0$ to $30d_0$. Interpretation of these results is left for next year (FY24), which will focus more on the BHR turbulence models.

5 Summary

The effects of computational parameters on xRAGE-BHR simulations of turbulent round jets with coflow were studied. The parameters include boundary conditions, mesh, domain size and timestep size. The inlet and outlet boundary conditions were modified within the framework of the freeze boundary condition to allow using the reflective boundary condition at the side wall. Five different non-AMR, static meshes were used to demonstrate that the flow quantities of interest are mesh-independent. Three different domain sizes were utilized to show that the flow quantities of interest are domain size-independent, and therefore not much affected by the wave reflections at the outlet. Results from simulations with four different CFL numbers show the solutions converging as the timestep size is reduced. Some preliminary results were presented which compare the BHR 2 and 3.1 model predictions with the experimental data. Effects of the initial turbulence length scale on model predictions were preliminarily examined with three different length scales. Lastly, it was found that the BHR 3.1 model solution exhibits a strange behavior of the mean axial velocity very close to the axisymmetry line.

6 Future Work (FY24)

With this year's demonstrated solution independence from different computational parameters, the focus of next year's (FY24) work will be twofold. First is to investigate the cause of the dip in the V profile at the symmetry axis when the BHR 3.1 model is used in an axisymmetric jet simulation. Second is to understand the causes of discrepancies between model predictions and experimental data. This will involve examination of turbulence budgets, and possibly the dissipation (or turbulence length scale) equation.

References

[1] Didier Besnard, Francis H. Harlow, Rick M. Rauenzahn, and Charles Zemach. Turbulence transport equations for variable-density turbulence and their relationship to two-field models. Technical Report LA–12303–MS, Los Alamos National Laboratory, 1992.

[2] K. Stalsberg-Zarling and R. Gore. The BHR2 turbulence model: Incompressible isotropic decay, Rayleigh-Taylor, Kelvin-Helmholtz and homogeneous variable-density turbulence. Technical Report LA–UR–11–04773, Los Alamos National Laboratory, 2011.

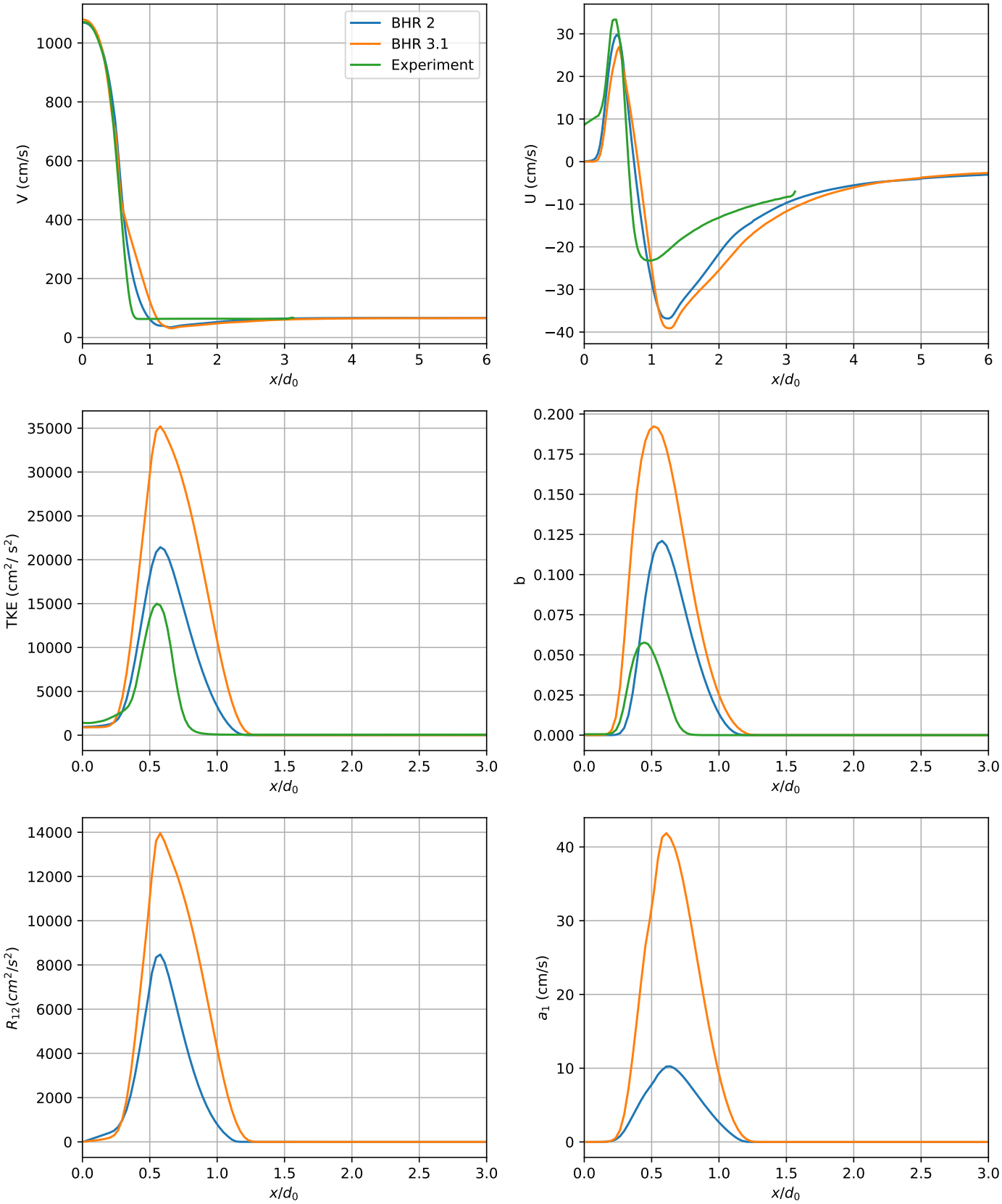

Figure 22: Radial profiles of flow variables V, U, TKE and b at $2d_0$ downstream of the nozzle exit. Shown are the BHR 2 and BHR 3.1 results, as well as experimental data.

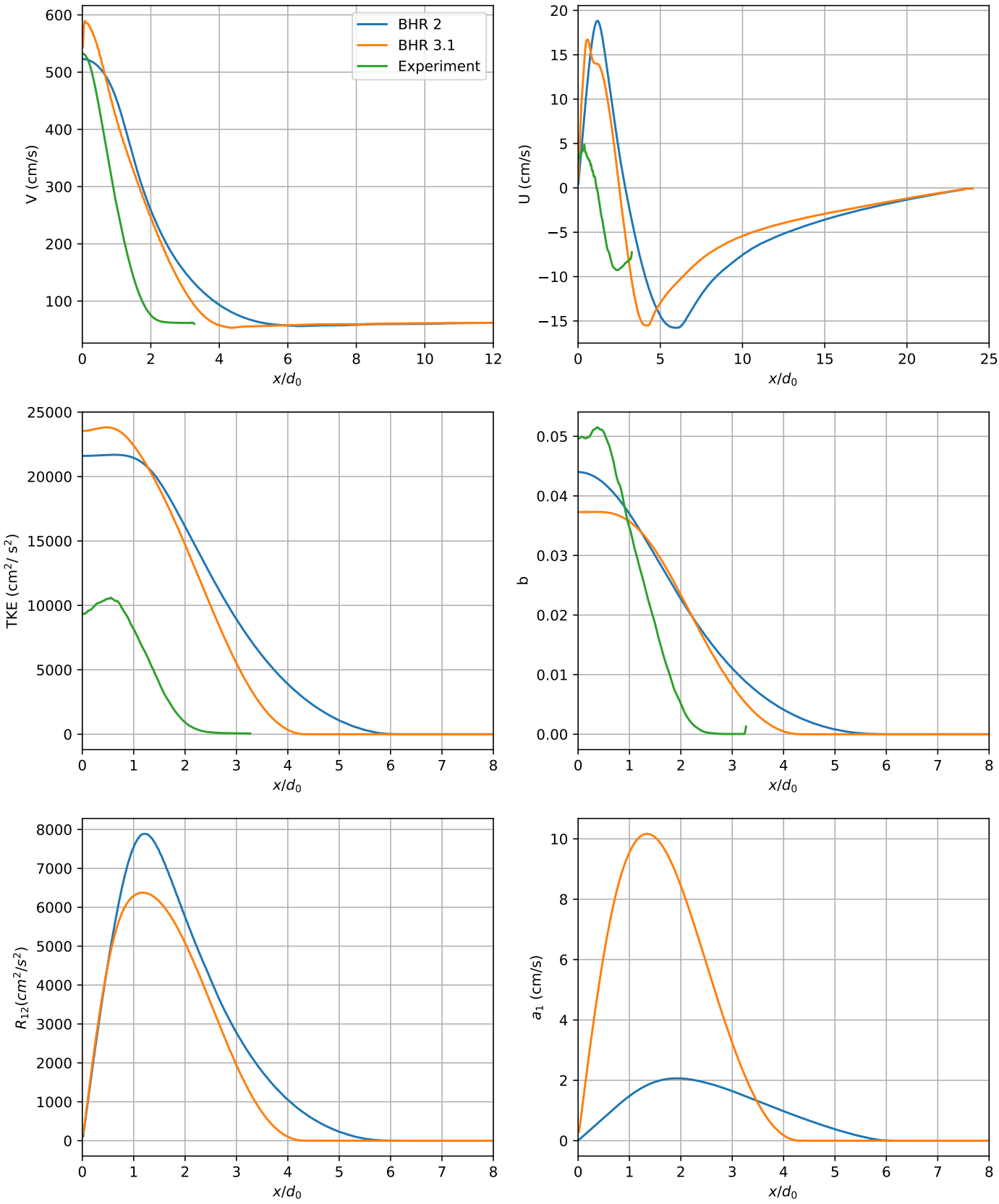

Figure 23: Radial profiles of flow variables V, U, TKE and b at $16d_0$ downstream of the nozzle exit. Shown are the BHR 2 and BHR 3.1 results, as well as experimental data.

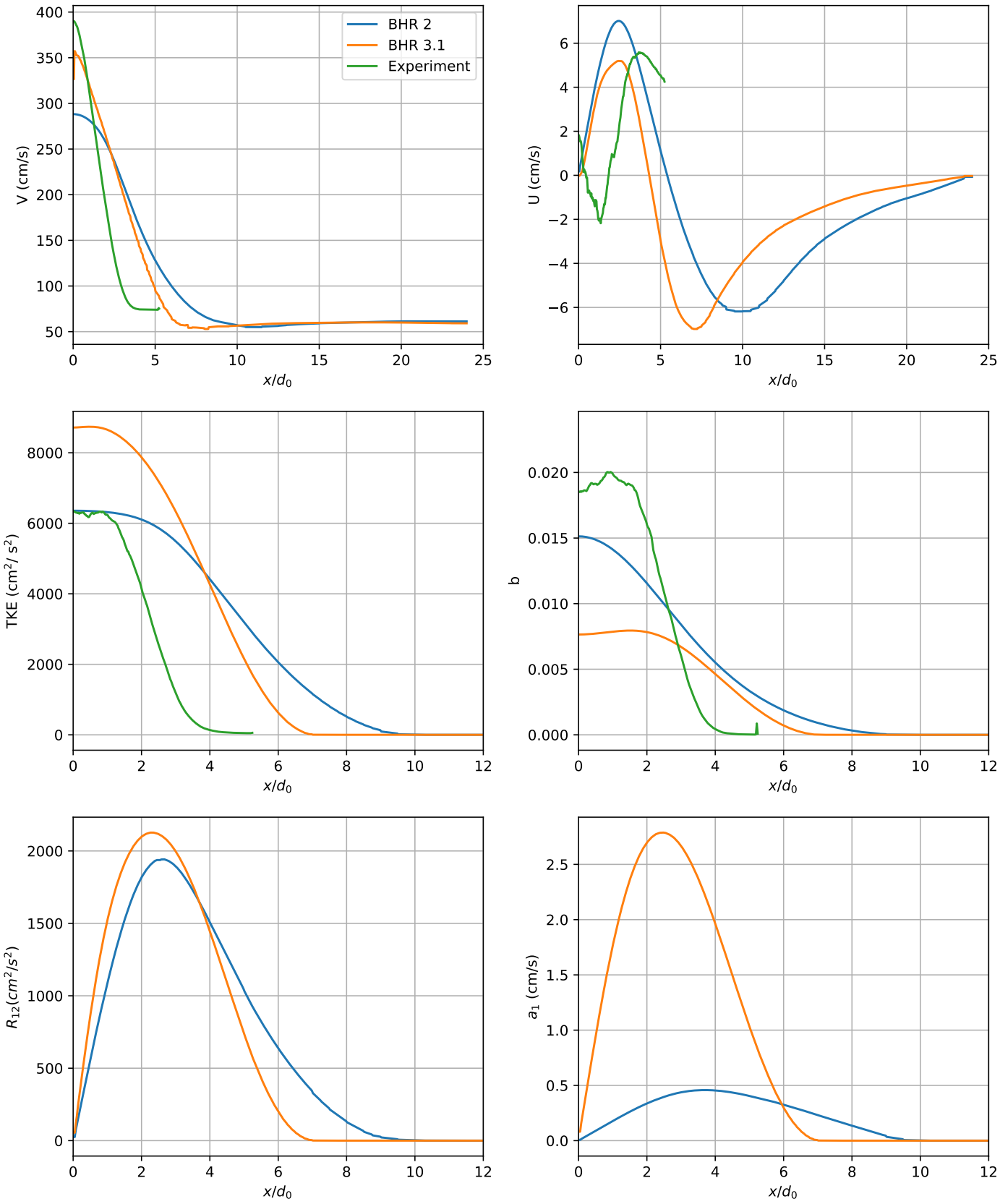

Figure 24: Radial profiles of flow variables V, U, TKE and b at $30d_0$ downstream of the nozzle exit. Shown are the BHR 2 and BHR 3.1 results, as well as experimental data.

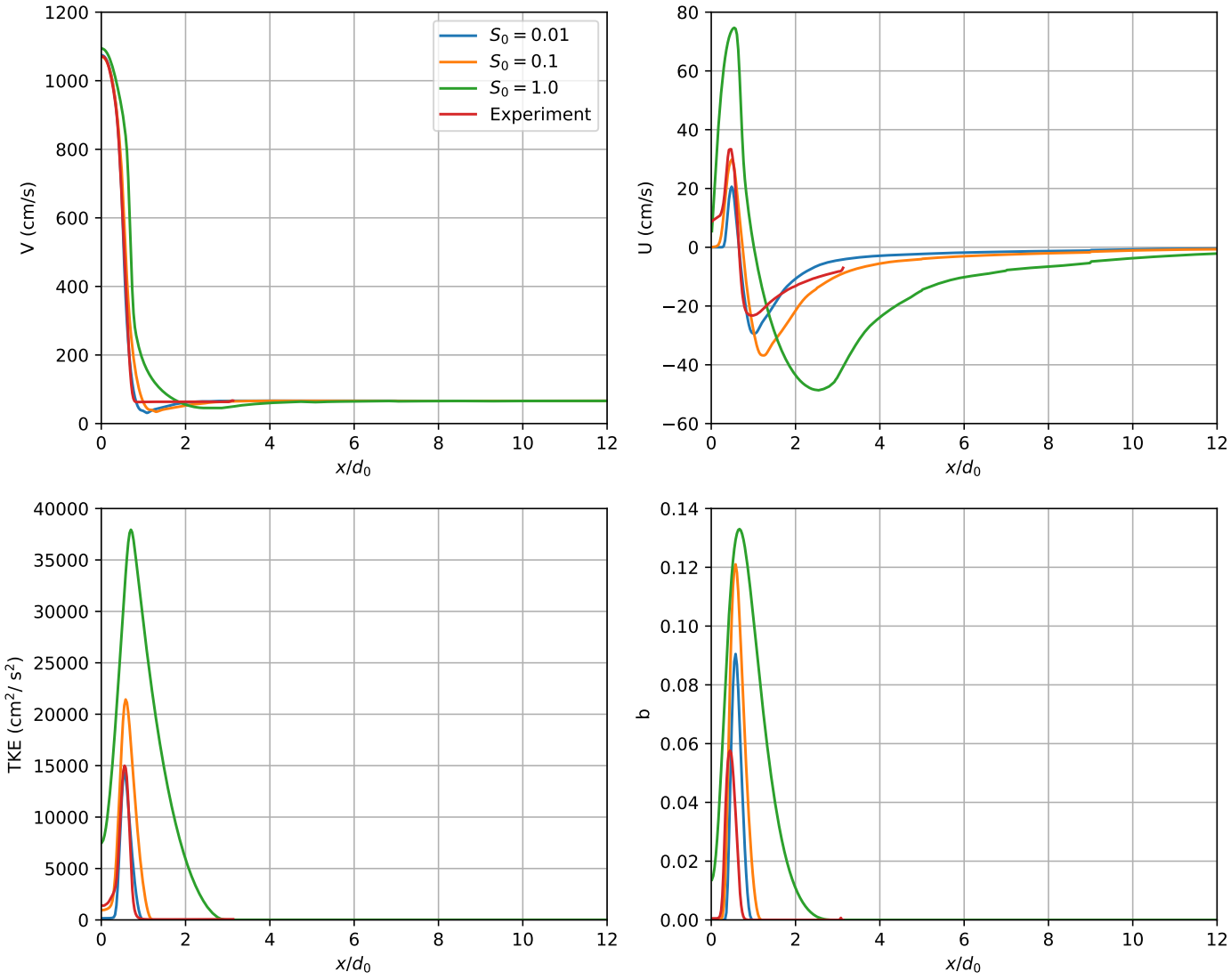

Figure 25: Radial profiles of flow variables V, U, TKE and b at $2d_0$ downstream of the nozzle exit from BHR 2 simulations with three initial length scales S_0, 0.01, 0.1 and 1.0. Also shown are the experimental data.

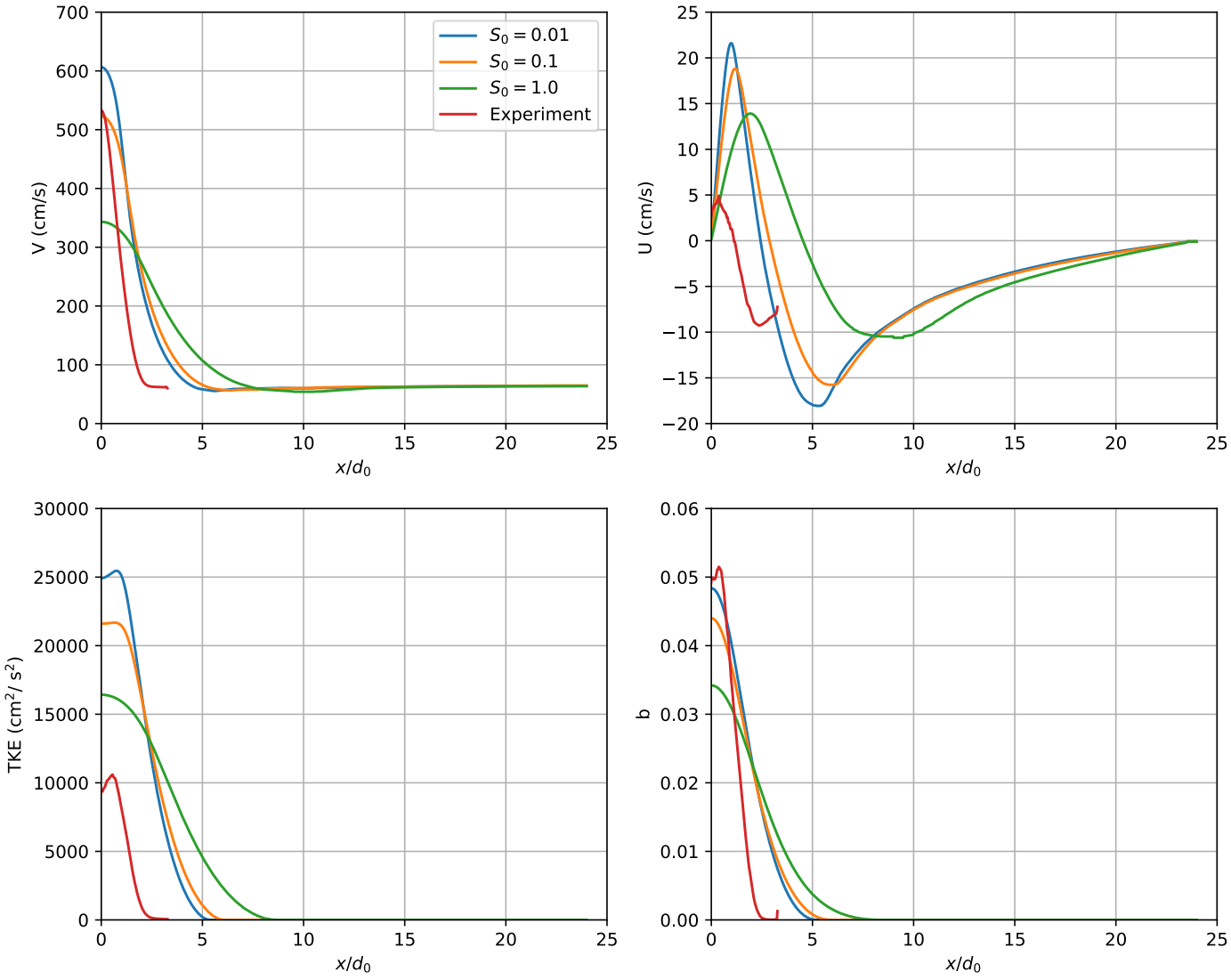

Figure 26: Radial profiles of flow variables V, U, TKE and b at $16d_0$ downstream of the nozzle exit from BHR 2 simulations with three initial length scales S_0, 0.01, 0.1 and 1.0. Also shown are the experimental data.

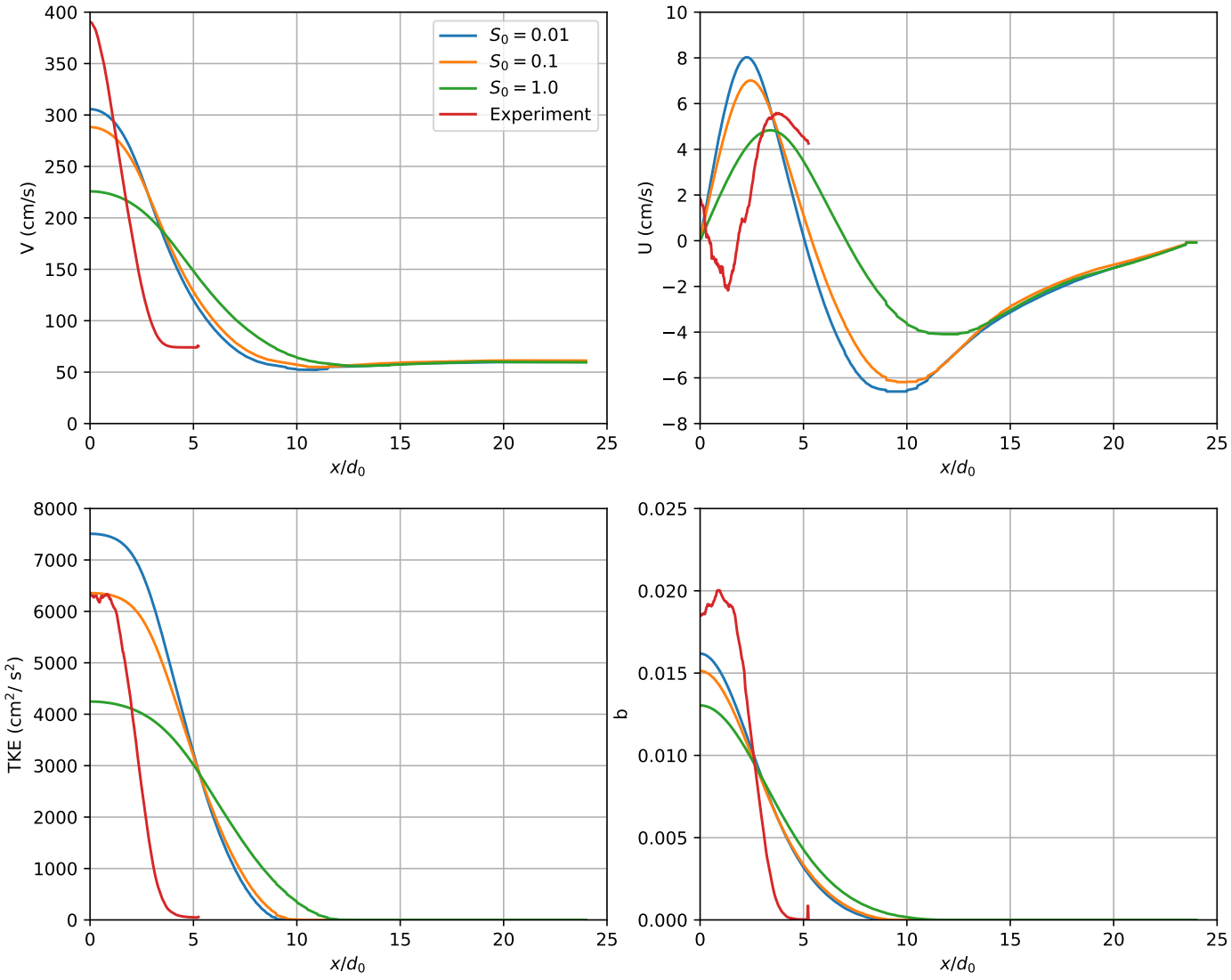

Figure 27: Radial profiles of flow variables V, U, TKE and b at $30d_0$ downstream of the nozzle exit from BHR 2 simulations with three initial length scales S_0, 0.01, 0.1 and 1.0. Also shown are the experimental data.

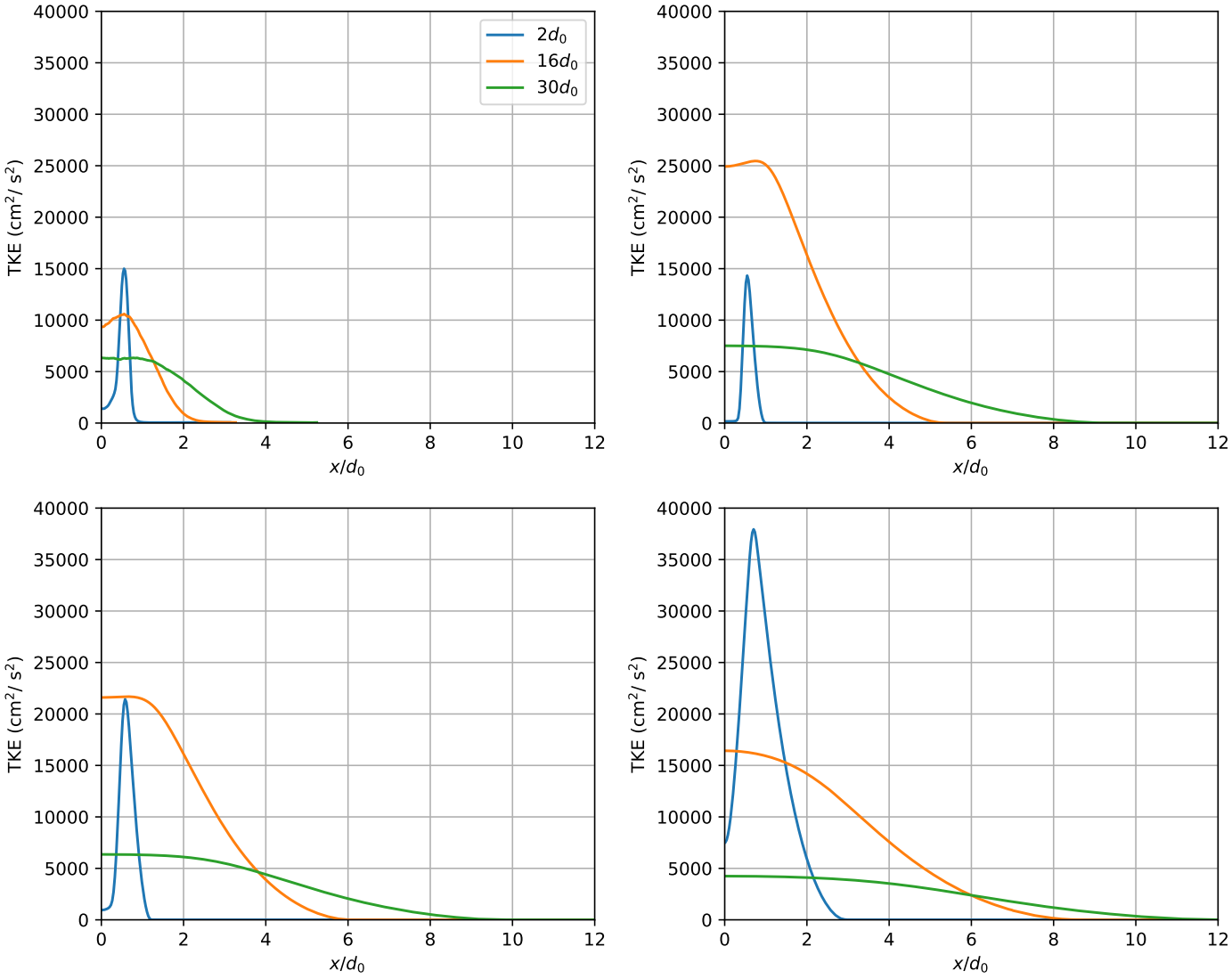

Figure 28: Radial profiles of TKE from BHR 2 simulations at three downstream locations $2d_0$, $16d_0$ and $30d_0$. The four plots correspond to experimental data (top left), $S_0 = 0.01$ (top right), $S_0 = 0.1$ (bottom left) and $S_0 = 1.0$ (bottom right), respectively.

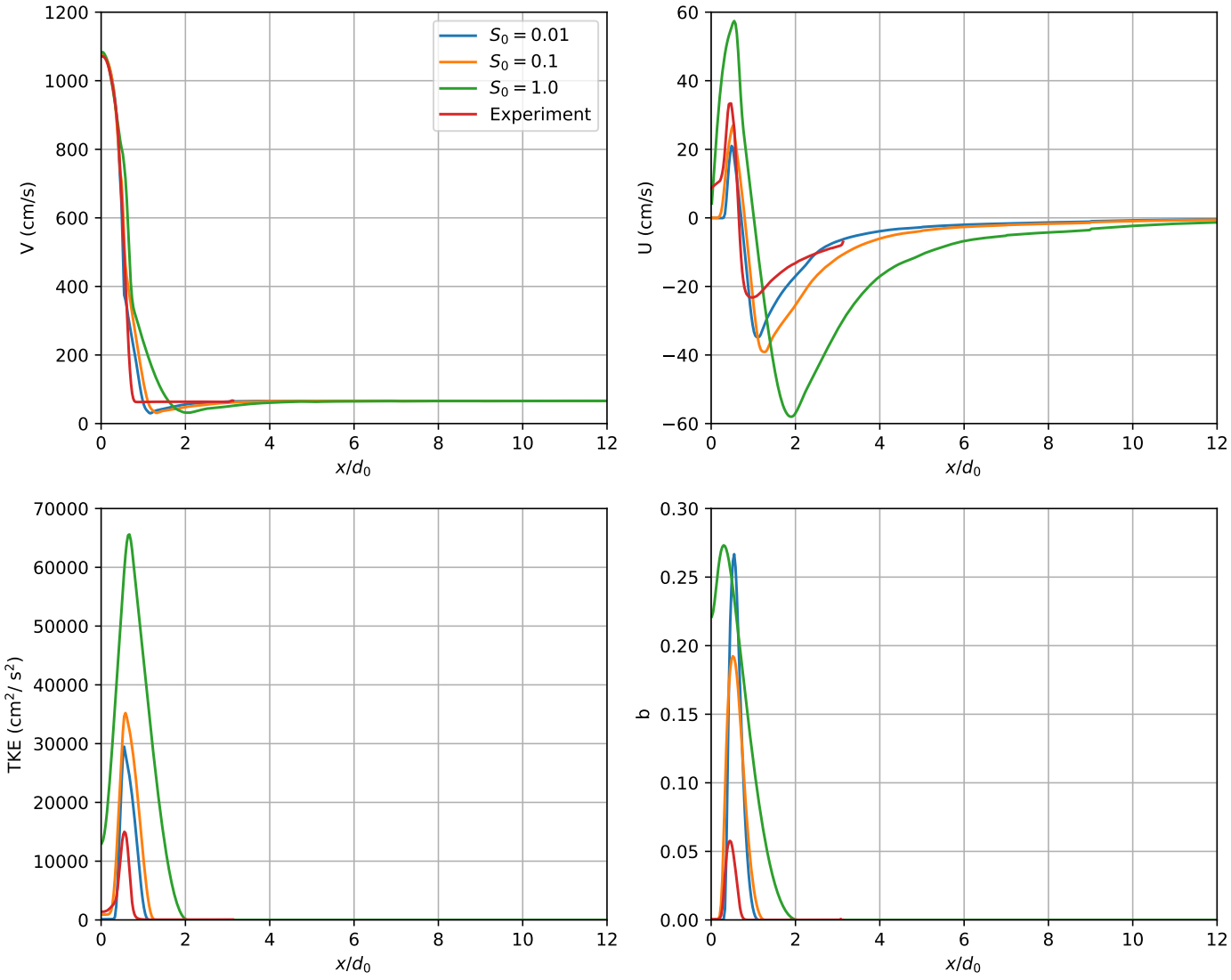

Figure 29: Radial profiles of flow variables V, U, TKE and b at $2d_0$ downstream of the nozzle exit from BHR 3.1 simulations with three initial length scales S_0, 0.01, 0.1 and 1.0. Also shown are the experimental data.

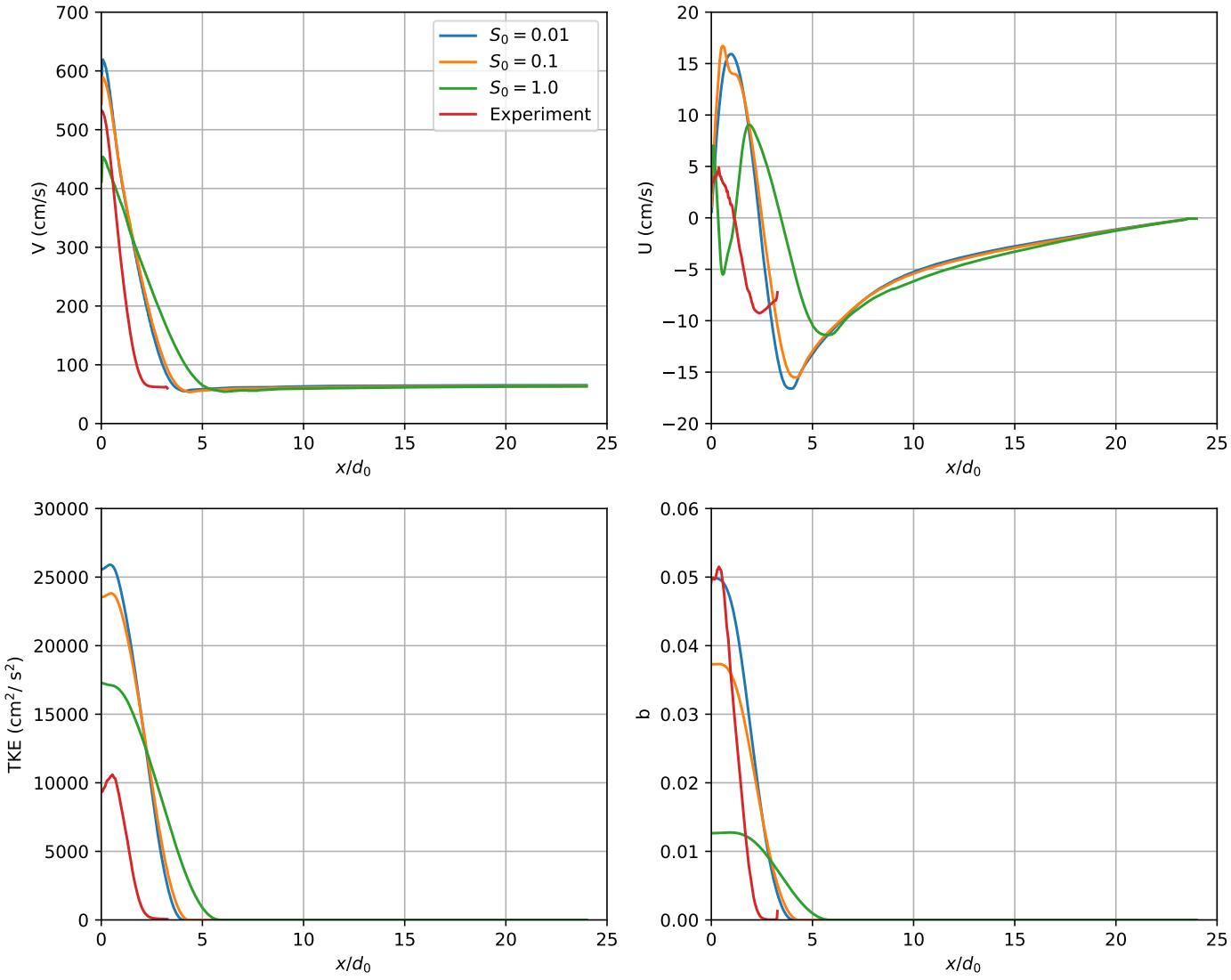

Figure 30: Radial profiles of flow variables V, U, TKE and b at $16d_0$ downstream of the nozzle exit from BHR 3.1 simulations with three initial length scales S_0, 0.01, 0.1 and 1.0. Also shown are the experimental data.

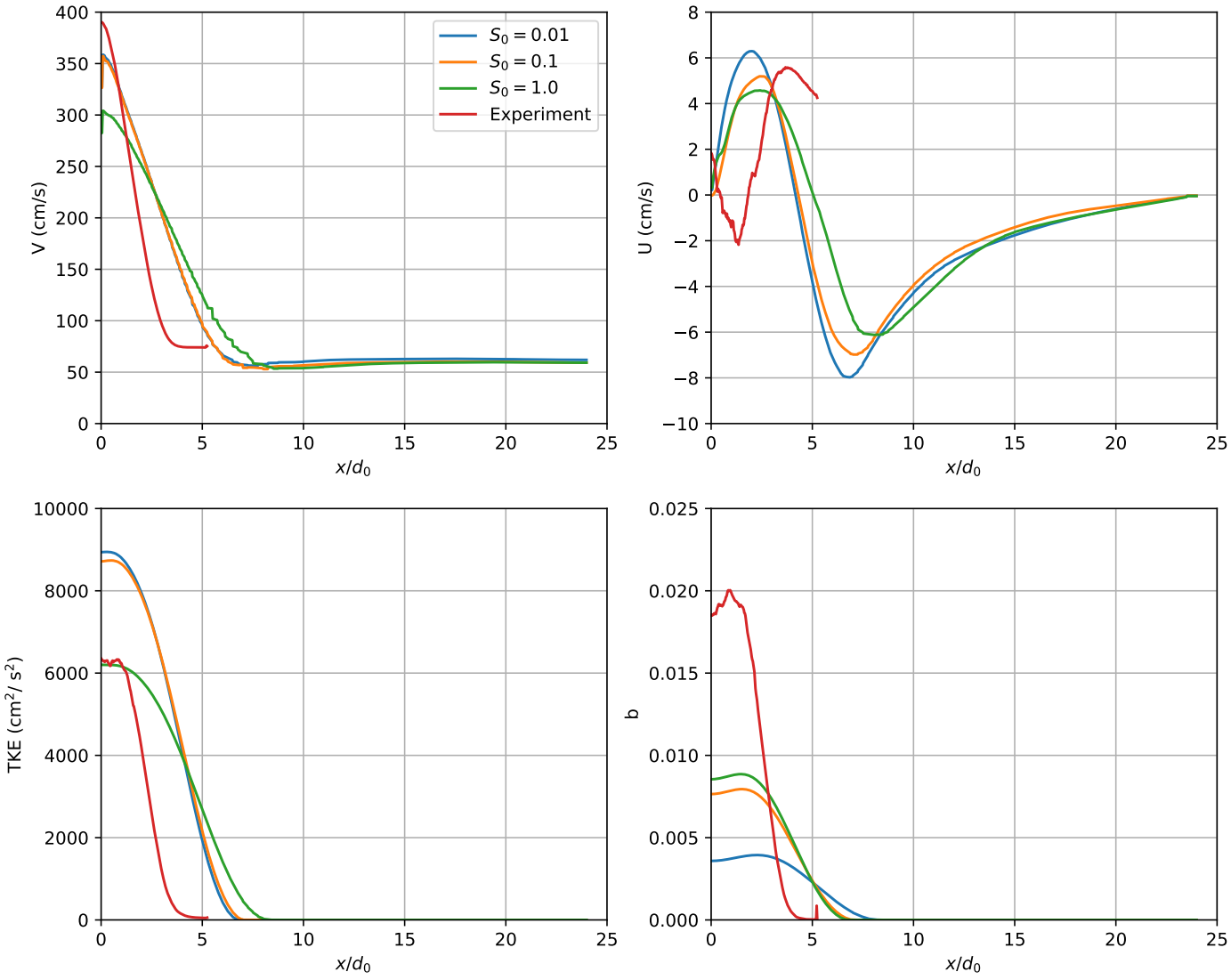

Figure 31: Radial profiles of flow variables V, U, TKE and b at $30d_0$ downstream of the nozzle exit from BHR 3.1 simulations with three initial length scales S_0, 0.01, 0.1 and 1.0. Also shown are the experimental data.

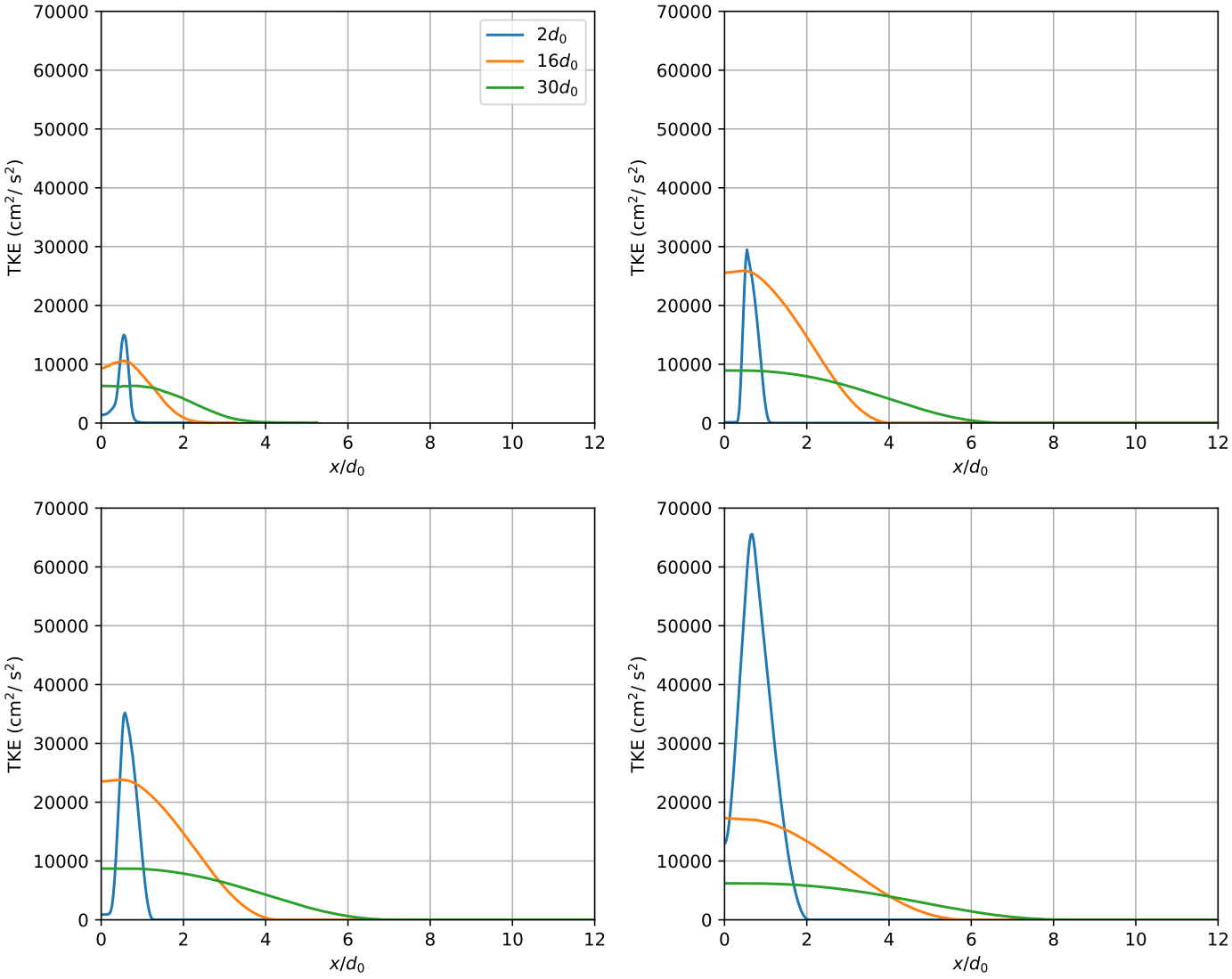

Figure 32: Radial profiles of TKE from BHR 3.1 simulations at three downstream locations $2d_0$, $16d_0$ and $30d_0$. The four plots correspond to experimental data (top left), $S_0 = 0.01$ (top right), $S_0 = 0.1$ (bottom left), $S_0 = 1.0$ (bottom right), respectively.

[3] John D. Schwarzkopf, Daniel Livescu, Robert A. Gore, Rick M. Rauenzahn, and J. Raymond Ristorcelli. Application of a second-moment closure model to mixing processes involving multicomponent miscible fluids. *Journal of Turbulence*, 12(49):1–35, 2011.

[4] J. D. Schwarzkopf, D. Livescu, J. R. Baltzer, R. A. Gore, and J. R. Ristorcelli. A two-length scale turbulence model for single-phase multi-fluid mixing. *Flow, Turbulence and Combustion*, 96:1–43, 2016.

[5] John J. Charonko and Katherine Prestridge. Variable-density mixing in turbulent jets with coflow. *Journal of Fluid Mechanics*, 825:887–921, 2017.

[6] Daniel Israel. FY 20 Variable density jet simulations: Final report, September 2019.

[7] Juan A. Saenz and R. Rauenzahn. Preparing xRAGE BHR for simulating axisymmetric jets. Technical Report LA–UR–20–30342, Los Alamos National Laboratory, September 2020.

[8] Michael Brent Cline. Jet project status end of year update, October 2021.

[9] Michael Brent Cline. Jet project status end of year update, January 2023.

[10] Michael Gittings, Robert Weaver, Michael Clover, Thomas Betlach, Nelson Byrne, Robert Coker, Edward Dendy, Robert Hueckstaedt, Kim New, W Rob Oakes, Dale Ranta, and Ryan Stefan. The rage radiation-hydrodynamic code. *Computational science & discovery*, 1, 2008.

[11] T.J. Poinsot and S.K. Lele. Boundary conditions for direct simulations of compressible viscous flows. *Journal of computational physics*, 1992.

[12] Fernando F. Grinstein. Open boundary conditions in the simulation of subsonic turbulent shear flows. *Journal of computational physics*, 115:43–55, 1994.

[13] F. F. Grinstein, R. H. Guirguis, J. P. Dahlburg, and E.S. Oran. *Three-dimensional numerical simulation of compressible, spatially evolving shear flows*. Lecture notes in physics. Springer-Verlag, 1989.

[14] S.B. Pope. An explanation of the turbulent round-jet/plane-jet anomaly. *AIAA journal*, 16(3), 1978.